Correlations between photocatalytic activity and chemical structure in copper doped TiO$_2$-SiO$_2$ with Cu^{2+} sites

Tihana Čižmar

University of Nova Gorica, Vipavska 13, SI-5000 Nova Gorica

Abstract

Copper modified TiO$_2$-SiO$_2$ photocatalysts were prepared by sol-gel method based on organic Cu, Si and Ti sources. Cu concentration varied from 0.1 to 3 mol%. The photocatalytic activity of the Cu modified TiO$_2$-SiO$_2$ catalyst was measured by oxidation of terephthalic acid (TPA), as a model pollutant. The results suggest that there is a ten times increase in photocatalytic activity when TiO$_2$-SiO$_2$ matrix was modified with 0.1 mol% of Cu. Crystal structure of Cu modified TiO$_2$-SiO$_2$ was analysed with XRD. Structural information on the incorporation of Cu cation in the crystal structure of TiO$_2$-SiO$_2$, and its chemical state in the coating, is determined with Cu K-edge EXAFS and XANES analysis. Results show that photocatalytic activity enhancement is due to Cu^{2+} cations attachment on the surface of photocatalytically active TiO$_2$ nanoparticles.

Keywords: Cu modified TiO$_2$-SiO$_2$ photocatalysts, titanium dioxide, metal doping, Cu K-edge XANES, EXAFS, photocatalytic activity

1. Introduction

Recent decades, research on photocatalytic materials has been a field of continuous expansions. As evidence, large number of articles was published every year. To this figure, it is necessary to add the combinations with other functional materials or between different semiconductors, as well as their morphological modifications. Different preparation strategies lead to enormous number of photocatalytic systems. Various studies

---

proved that TiO_2 is the most efficient and environmentally benign photocatalyst [1]. Improved photocatalytic properties have been found for TiO_2-SiO_2 nanostructured coatings used in environmental applications [2]. The coatings have good antifogging, self-cleaning and antimicrobial surfaces due to their photocalytic properties and photoinduced superhydrophilicity [3]. To reduce high rate of recombination between photogenerated electrons and holes in TiO_2-SiO_2, metal doping was introduced [4]. An appropriate amount of transition metal ions doped into TiO_2-SiO_2 can introduce electron capture centers, and may as well change the crystallinity of TiO_2, resulting in a decrease in electron/hole recombination centers [5]. The metal ion doping of TiO_2 has been able to induce the spectral shifts into the visible light region [6, 7]. The photocatalytic activity is improved if Pt, Pd, Au or Ag are used as dopants [8], but these metals are rare and expensive. It was found that addition of copper can, in some cases, improve the photocatalytic activity [9], but the mechanism responsible for the improvement is not yet explained. Novel Cu modified TiO_2-SiO_2 materials have promising photocatalytic properties, they can be cheaper and more efficient. The main purpose of this research is to improve the photocatalytic activity of Cu modified TiO_2-SiO_2 photocatalyst used for the degradation of organic pollutants in an aqueous medium with solar energy source. New sol-gel synthesis path, based on organic Cu, Si and Ti precursors, is used to prepare improved Cu modified TiO_2-SiO_2 photocatalyst with varied Cu concentrations ranging from 0.1 to 3 mol%. Cu K-edge XANES and EXAFS analysis was used to precisely determine local structure of Cu cations in TiO_2-SiO_2 photocatalyst, to identify the correlations between the Cu cation structure and photocatalytic activity of the Cu modified TiO_2-SiO_2 materials, and to clarify the mechanism responsible for improved activity.

2. Experimental methods

2.1. Synthesis of Cu modified TiO_2-SiO_2 photocatalysts

Sol-gel method was used to synthesize new copper modified TiO_2-SiO_2 photocatalysts with varied dopant concentrations (0.1 and 3 mol%), using titanium tetraisopropoxide (TTIP), tetraethyl ortosilicate (TEOS) and colloidal SiO2, and copper acetlyacetonate ($Cu(acac)_2$) as Ti, Si and Cu sources. We modified the known synthesis path [3]. For the TiO_2-SiO_2 colloidal solution we prepared silica binder solution from 1.11 mL tetraethyl ortosilicate (TEOS, Acros Organics), 1.7 mL colloidal SiO_2 Levasil (Obermeier) 200/30% aqueous solution, 30 μL HCl (32 wt%, J.T. Baker) to catalyse TEOS

hydrolysis, and after 1h of mixing 5 mL 1-propanol (Fluka) was added. The obtained product contained 11.5 wt% of SiO_2. The TiO_2 sol was prepared by dissolving titanium tetraisopropoxide (TTIP, Acros Organics) (15 mL) in absolute ethanol (2.5 mL). In the first step, double deionized water (45 mL) and 70% perchloric acid (1 mL) were mixed separately. This solution was then added to the TTIP solution drop-wise, under reflux and heating, where exothermic reaction of uncontrolled hydrolysis and condensation of TTIP took place, gaining white precipitate of hydratised amorphous TiO_2. After heating and refluxing for 48 h, a stable translucent TiO_2 sol was obtained. The TiO_2-SiO_2 sol (denoted TS) was obtained by adding silica binder solution (3 mL) to TiO_2 sol (3 mL) The sol was further diluted with 4 mL double deionized water and organic solvents (6 mL of 1-propanol and 19.5 mL of 2-propoxyethanol). Copper cations were added by direct incorporation during the sol-gel synthesis. $Cu(acac)_2$ (200 mg) dissolved in 2-propoxyethanol (150 mL), used as a source of copper, was added (600 µL, 18 mL) into the TiO_2-SiO_2 sol. All TiO_2-SiO_2 sols (unmodified and Cu modified) were dried at 150 °C for 1 h, to obtain unmodified TiO_2-SiO_2 and Cu modified TiO_2-SiO_2 catalysts with two different dopant concentrations (0.1 and 3 mol%), denoted as TS_150, TS_0.1Cu_150, TS_3Cu_150, respectively. In addition, another set of photocatalyst samples (TS_500, TS_0.1Cu_500, TS_3Cu_500) was prepared from the dried photocatalysts, by calcination of the dried powders at 500 °C for 1 h.

2.2. Photocatalytic activity

Photocatalytic activity of Cu modified TiO_2-SiO_2 catalysts was tested by degradation of terephthalic acid (TPA), as a model pollutant, using a highly sensitive fluorescence-based detection method [10]. Two solutions were prepared, stock solution of Terephthalic acid (TPA) (2 mL) with the concentration of 130 mg/L, and working solution of TPA (100 mL) with the concentration of 83 mg/L. 25 mL of TPA and 10 mg of photocatalyst were mixed in 25 mL of double deionized water and stirred under sunlight irradiation. Samples (1 mL) of the water solution were taken from the reactor at different UV irradiation times (0 min, 3 min, 6 min, 10 min, and 20 min) and centrifuged (1300 min^{-1}) for 3 min. A fixed volume (159 µL) of the solution was then sampled with an automatic pipette, and transferred into microliter plate wells (microliter plate with 96 wells, flat bottom, black) for fluorescence measurements. Photocatalytic tests were carried out in solar simulator (Suntest XLS+, Atlas, USA) chamber with a simulated solar irradiation source (Xenon lamp), using daylight filter, at UV light flux of 750

3

W/m2. During irradiation in the presence of the photocatalyst the TPA is decomposed and highly fluorescent 2-hydroxyterephthalic acid (HTPA) is formed as an intermediate oxidation product. Fluorescence measurements were performed using a microplate reader in the fluorescence mode (Infinite F200 Microplate reader, Tecan, Switzerland). The wavelength of the excitation light was 320 nm (filter bandwidth: 25 nm) and emission was measured at 430 nm (filter bandwidth: 35 nm). The instrument was operating in top mode with 25 reads per well, with 20 μs integration time. The amplification factor for the photomultiplier tube was 56 or 78. For each irradiation time, at least four parallel photocatalytic tests were done. Oxidation of TPA to HTPA under UV/Vis irradiation can be described by zero-order kinetics, (rate constant k_1). For the subsequent degradation of HTPA, the pseudo-first order kinetics (rate constant k_2) is proposed [10],

$$\frac{d[HTPA]}{dt} = k_1 - k_2 \tag{1}$$

which predicts the following time dependence of the concentration of HTPA with time of the UV illumination of TPA in the presence of the photocatalyst in the water:

$$[HTPA] = \frac{k_1}{k_2}(1 - e^{-k_2 t}) \tag{2}$$

Measurements of HTPA concentrations were performed in the time interval from 0 to 20 minutes. Due to a small value of the rate constant k_2 (t $\ll 1/k_2$), we can approximate the exponential term in Eq. 2 with a linear approximation (1-$k_2 t$) and model the time dependence of the HTPA concentration with a linear function:

$$[HTPA] = k_1 t \tag{3}$$

The formation rate constant of HTPA (k_1) is used to compare photocatalytic activity of the Cu modified photocatalysts with an unmodified one.

2.3. XRD analysis

Crystal structures in unmodified and Cu modified TiO$_2$-SiO$_2$ samples were identified by X-ray diffraction (MiniFlex Benchtop 300/600, 150) using Cu *Kα* irradiation from 10 to 80 ° at a scan rate of 2°/min. Quantitative phase composition analysis was performed using Rietveld refinement

method by the High Score Plus software. The crystallite size was determined from XRD pattern, using Sherrer formula:

$$d = \frac{0.9\lambda}{\beta cos\theta} \qquad (4)$$

where d is in nm, λ the wavelength of X-ray in $\mathring{A}$ (1.5418 $\mathring{A}$), β full width at half maxima (FWHM) of diffraction peak(s) in radians, and θ is the Bragg angle.

2.4. N_2 - physisorption

Nitrogen adsorption measurements were performed at -196.15 °C on a Tristar 3000 Micromeritics volumetric adsorption analyser. Before the adsorption analysis, the samples were outgassed under vacuum for 2 h at 473 K in the port of the adsorption analyser. The BET specific surface area [11] was calculated from adsorption data in a relative pressure range from 0.05 to 0.25. The total pore volume was estimated on the basis of the amount adsorbed nitrogen at a relative pressure of 97% [12]. The pore size distributions (PSDs) were calculated from nitrogen adsorption data using a BJH algorithm. [13]. The maxima on the PSD are considered as the primary mesopore diameters for given samples.

2.5. XAS

The local structure and chemical state of copper cations in Cu modified TiO_2-SiO_2 photocatalyst was analysed by X-ray absorption spectroscopy. Cu K-edge absorption spectra of photocatalyst samples, and 0.005 M liquid solution $Cu(acac)_2$ dissolved in 2-propoxyethanol used as copper source, were measured at room temperature in transmission or fluorescence detection mode at the XAFS beamline of the ELETTRA synchrotron radiation facility in Trieste, Italy. The Cu modified TiO_2-SiO_2 samples were prepared as powder pellets, while the liquid sample was inserted in the liquid absorption cell with 0.5 mm thick Plexiglas windows. In all cases the total absorption thickness of the sample was about 2 above the Cu K-edge. A Si (111) double crystal monochromator was used with energy resolution of 1 eV at Cu K-edge. Higher-order harmonics were effectively eliminated by detuning the monochromator crystals to 80% of the rocking curve maximum. The intensity of the monochromatic X-ray beam was measured by three consecutive 30 cm long ionization detectors respectively filled with

5

following gas mixtures: 1250 mbar N_2, 750 mbar He; 250 mbar Ar, 750 mbar He, 1000 mbar N_2; 700 mbar Ar, 1000 mbar N_2, 300 mbar He. The absorption spectra were measured in the energy region from -150 eV to +1000 eV relative to the Cu K-edge. In the XANES region equidistant energy steps of 0.25 eV were used, while for the EXAFS region equidistant k steps of 0.03 $Å^{-1}$ were adopted, with an integration time of 1 s/step for transmission measurements. For samples with low Cu concentration, fluorescence detection mode was used, with SDD fluorescence detector with integration time of 5s/step. Three to eight repetitions of the scans were superimposed to improve signal-to-noise ratio. The exact energy calibration was established with simultaneous absorption measurement on a 5-micron thick Cu metal foil placed between the second and the third ionization chamber. Absolute energy reproducibility of the measured spectra was $\pm$ 0.03 eV. The quantitative analysis of EXAFS spectra is performed with the IFEFFIT program package [14] in combination with FEFF6 program code [15] for ab initio calculation of photoelectron scattering paths.

3. Results and discussion

3.1. Photocatalytic activity measurements

The photocatalytic activity of Cu modified TiO_2-SiO_2 catalysts during UV/Vis illumination is measured by degradation of TPA, where HTPA is formed as an intermediate product. HTPA concentration as function of UV/Vis illumination time is shown on Fig. 1. The TPA degradation rate constant k_1 is determined with the theoretical model (Eq. 1) by best fit. Best fit values of k_1 for each sample are presented in Table 1. The results suggest that there is a ten times increase in photocatalytic activity when TiO_2-SiO_2 matrix is modified with 0.1 mol% of Cu, while at other doping concentrations samples exhibit similar (within errorbars) or smaller photocatalytic activity compared to unmodified reference sample.

3.2. N_2 - physisorption

Specific surface area of unmodified and Cu modified TiO_2-SiO_2, determined using nitrogen adsorption and desorption analysis is given in Table 1. The largest specific surface area is found in TS_0.1Cu_150, which is slightly higher than in the reference TS_150 sample. The sample with highest specific surface area is the most photocatalytically active, confirming beneficial influence of specific surface area on activity of the catalyst.
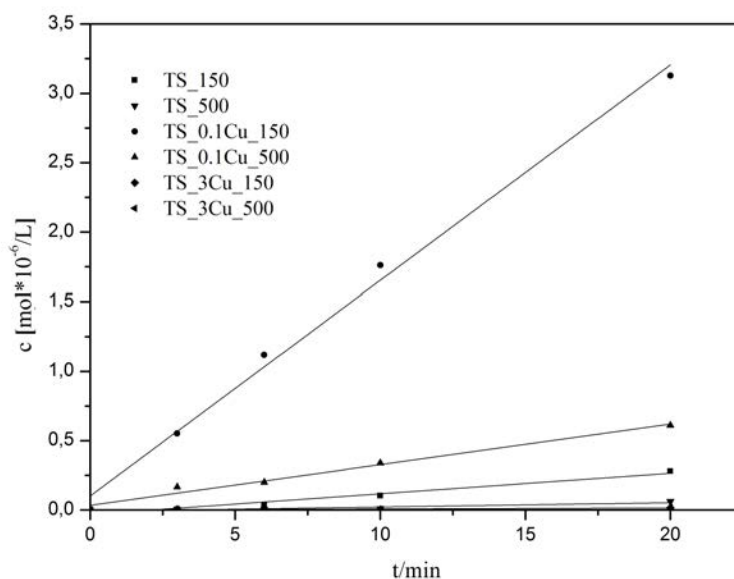
Figure 1: HTPA concentrations as function of UV/Vis illumination time for unmodified and Cu modified TiO_2-SiO_2 powder catalysts with different dopant concentrations (0.1 and 3 mol%). (Dots - experiment, solid line - best fit model (Eq. 1))

TS_3_Cu_150 sample has the smallest surface area. After calcination at 500 °C the surface area does not significantly change in any of the samples. There are only minor differences in average pore size between all samples.

Type of photocatalyst	Specific surface area / m^2g^{-1}	Average pore size / nm	k_1 / $10^{-6}Mmin^{-1}$	Relative photoactivity (%)
TS_150	274.5	4.3	0.015(2)	1
TS_500	271.1	4.6	0.0031(7)	0.2
TS_0.1Cu_150	292.9	3.9	0.155(7)	10.3
TS_0.1Cu_500	291.3	4.2	0.029(2)	1.9
TS_3Cu_150	224.4	4.1	0.0007(2)	0.05
TS_3Cu_500	274.2	4.3	0.0006(2)	0.04

Table 1: Specific surface area, average pore size, and the TPA oxidation rate constant k_1 of unmodified TiO_2-SiO_2 dried at 150 °C (TS_150) and Cu modified TiO_2-SiO_2 samples dried at 150 °C, and samples additionally calcinated at 500 °C. Relative photoactivity (%) of the photocatalysts, i.e. k_1 constant of the photocatalyst compared to the k_1 constant of the reference unmodified TS_150 photocatalyst is given in the last column.

7

3.3. XRD results

Anatase is the major crystal phase in all samples, with a minor amount of brookite phase. The broad peak that appears at 2θ around 22° can be attributed to glass-like amorphous silicate nanoparticles. No other crystalline species were detected. For the pure TiO_2-SiO_2 sample, the final quantitative analysis resulted in the composition of 77% of anatase and 23% of brookite, with the crystallites size of 2.7 nm and 5.2 nm, respectively. Samples with different Cu concentrations at 150 °C and at 500 °C contain the same crystalline structure as unmodified TiO_2-SiO_2. The addition of Cu does not change the relative ratio between anatase and brookite phase. Diffraction peaks of the (101) anatase and (121) brookite planes for all samples were used to evaluate the lattice parameters as well as the crystal size. The parameters are listed in Table 2. There are no changes in the anatase and brookite crystal unit cell parameters and crystal sizes in Cu modified samples (dried and calcinated) compared to the unmodified sample.

Sample	Lattice parameters			Cell V / $\mathring{A}^3$	Cr. size / nm
	a	b	c		
TS_150	3.784	3.784	9.515	136.24	2.7
TS_500	3.797	3.797	9.579	138.10	2.7
TS_0.1Cu_150	3.785	3.785	9.520	136.39	2.7
TS_0.1Cu_500	3.785	3.785	9.514	136.30	2.7
TS_3Cu_150	3.789	3.789	9.537	136.39	2.7
TS_3Cu_500	3.785	3.785	9.520	136.39	2.7

Table 2: Lattice parameters and crystallite size of Cu doped TiO_2-SiO_2.

3.4. X-ray absorption spectroscopy

Analysis of Cu K-edge XANES spectra of the catalyst samples and reference compounds was performed with the IFEFFIT program package ATHENA [14]. The relative K-shell contribution in the absorption spectra (Fig. 2) is obtained by the standard procedure [16] by removing the extrapolated best-fit linear function determined in the pre-edge region (-150 eV -30 eV), and by conventional normalization, extrapolating the post-edge spline background, determined in the range from 100 to 860 eV, to set the Cu K-edge jump to 1. The valence state of the Cu cation can be determined from the Cu K-edge XANES, where the valence is known to directly affect the

shape and position of the edge features. The energy positions of Cu K-edge in all Cu modified TiO_2-SiO_2 samples and in the liquid $Cu(acac)_2$ precursor, correspond with the energy position of reference Cu^{2+} compounds (Fig. 2), so we can conclude that Cu cations in the photocatalysts are in divalent form. Different local environments of the Cu cation result in different K-edge profiles and pre-edge lines in the XANES spectra. Comparison of the XANES spectra of Cu modified TiO_2-SiO_2 samples reveals differences between dried samples and the sample additionally calcinated at 500 °C. In the calcined samples, a shoulder in the pre-edge region, attributed to 1s-4p excitation, indicates the formation of CuO phase. Comparison of the XANES spectra of dried photocatalysts at 150 °C with the XANES spectra of reference Cu^{2+} compounds shows that Cu^{2+} cation symmetry is different from that in the $Cu(acac)_2$ liquid precursor, that was used as a source of copper in the synthesis, and do not match any of the other reference compounds.
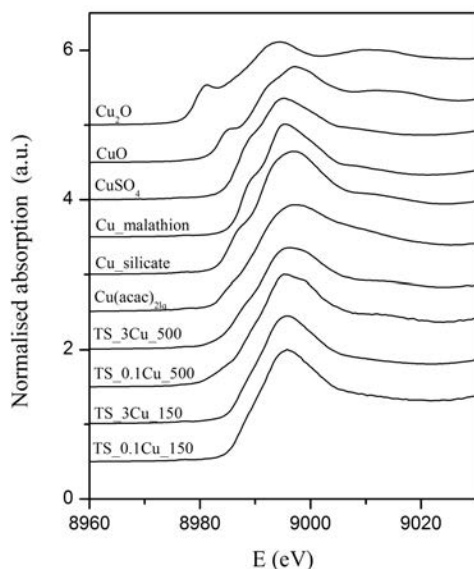

Figure 2: Normalized Cu K-edge XANES spectra, displaced vertically, of the TS_0.1Cu_150, TS_3Cu_150 samples after drying at 150 °C and calcinating at 500 °C. Reference Cu^+ and Cu^{2+} copper compounds with different Cu cation coordination (Cu_2O, CuO, $CuSO_4$, Cu malathion, Cu doped silicate, and liquid $Cu(acac)_2$ precursor) are shown for comparison.

A more detailed insight into the local structure around Cu atoms in the Cu modified TiO_2-SiO_2 samples can be obtained from the Cu K-edge EXAFS analysis. Fourier transforms of the k3 weighted EXAFS spectra of the samples and liquid Cu(acac)$_2$ precursor are shown in Fig. 3. The quantitative analysis of Cu K-edge EXAFS spectra were performed with the IFEFFIT program package [14]. Structural parameters were quantitatively resolved by comparing the measured signal with the simulated EXAFS spectra, constructed with the FEFF6 program code in which the photoelectron scattering paths are calculated ab initio from a tentative spatial distribution of neighbour atoms. The model was composed from six oxygen atoms in the first coordination shell distributed at two different distances, carbon or oxygen in the second coordination shell and Si, Ti, Cu, O neighbours at larger distances. The Fourier transforms spectra from the series (Fig. 3) reveal the contributions of consecutive shells of Cu neighbours of up to 3.9 Å. Very good fits are obtained in the k interval from 3 $Å^{-1}$ to 11 $Å^{-1}$, and the R range of 1 Å up to 3.3 Å. The list of best fit parameters is given in the Table 3. Two shells of neighbours are discerned in the local neighbourhood of Cu atoms in the liquid copper precursor (copper acetylacetonate dissolved in 2-propoxyethanol). A fit of the EXAFS spectrum in the k range of 3 $Å^{-1}$ to 11 $Å^{-1}$ and the R range of 1 Å to 3.3 Å showed that the Cu atom is coordinated with 4 O atoms at a distance of 1.94 Å and 2 O atoms at 2.03 Å, while the second shell of neighbours consists of carbon atoms at 2.89 Å and 3.09 Å. The local structure around Cu formed in the liquid precursor is not retained in samples dried at 150 °C (TS_0.1Cu_150, TS_3Cu_150). The fit of the EXAFS spectrum of the most active sample (TS_0.1Cu_150), in the k range of 3 $Å^{-1}$ to 11 $Å^{-1}$, and the R range of 1 Å to 3.1 Å, showed that the Cu atom is coordinated with 4 O atoms at distance of 1.94 Å, while the second shell of neighbours consists of carbon and titania atoms at 2.8 Å and 2.97 Å. The Cu-O-C connections detected in the liquid precursor are partially preserved after drying at 150 °C, however, a part of Cu cations forms Cu-O-Ti bridges. In the TS_3Cu_150 sample, a part of the Cu-O-C connections is preserved, but we detected that a part of Cu cations formed Cu-O-Cu dimers. There are no Cu-O-Ti connections present. The connection of Cu cations to the surface of TiO_2 nanoparticles in the TS_0.1Cu_150 sample is the key feature that distinguishes active from inactive samples, and can explain the increased photocatalytic activity of the TS_0.1Cu_150 photocatalyst. Cu cations, adsorbed on the surface of TiO_2 nanoparticles can introduce electron capture centers that promote charge separation, resulting in a decrease in the rate of electron/hole recombination in the TiO_2 photocatalyst. The structure around Cu cations changed significantly af-

ter calcination at 500 °C. Cu cations in the TS_0.1Cu_500, and TS_3Cu_500 samples, are coordinated with 6 O in the first neighbour shell, located at the same distances as in the liquid precursor, but their distribution around the Cu atom is significantly altered. Cu-O-Si bonding is present, which points to Cu incorporation in the SiO_2 matrix, and Cu-O-Cu bonding is identified, which indicates the formation of amorphous copper oxides. After calcination at 500 °C there are no Cu-O-Ti connections present in the structure, and consequently the beneficial role of copper cations, which can promote charge separation in TiO_2 photocatalytic particles, is lost.
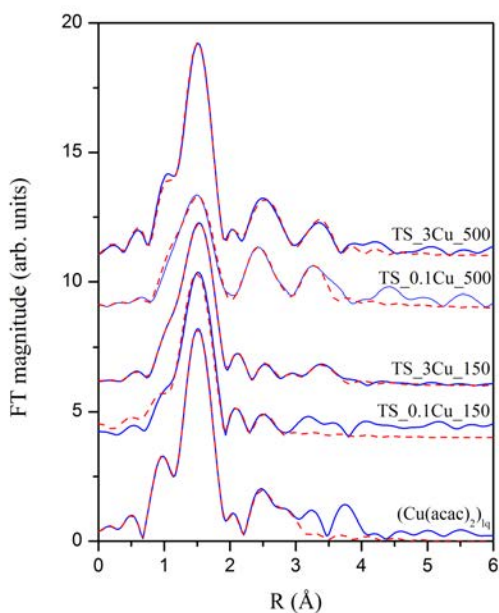
Figure 3: Fourier transform magnitudes of the k^3-weighted Cu EXAFS spectra of Cu modified TiO_2-SiO_2 calculated in the k interval from of 3 $Å^{-1}$ to 11 $Å^{-1}$, (blue solid line - experiment, red dashed line - EXAFS model)

Cu neighbour	N	$R/\text{Å}$	$\sigma^2 / \text{Å}^2$	R-factor
Cu(acac)2 liquid precursor				
O	4	1.94(1)	0.004(1)	
O	2	2.3(1)	0.020(5)	0.0001
C	4	2.89(3)	0.003(3)	
C	5(2)	3.09(9)	0.005(1)	
TS_0.1Cu_150				
O	3.7(5)	1.95(1)	0.004(1)	
C	2.5(3)	2.9(1)	0.006	0.0003
Ti	0.7(3)	3.1(1)	0.006	
TS_3Cu_150				
O	5.5(6)	1.98(1)	0.007	
O	1.1(5)	2.28(3)	0.008	
C	2.8(2)	2.57(5)	0.029(9)	0.00008
Cu	0.6(2)	3.31(3)	0.01	
O	3.5(8)	3.86(3)	0.008	
TS_0.1Cu_500				
O	2.9(4)	1.94(2)	0.006	
O	3.1(4)	2.49(4)	0.008	
O	2(1)	2.81(3)	0.008	0.006
Si	4(2)	3.17(3)	0.008	
Cu	3(2)	3.47(3)	0.009	
TS_3Cu_500				
O	4.7(4)	1.95(1)	0.006(1)	
O	1.2(4)	2.32(7)	0.008	
O	2(1)	2.90(3)	0.008	0.00005
Si	1.5(5)	3.18(3)	0.008	
Cu	2(1)	3.50(5)	0.009	
O	3(2)	3.77(3)	0.015	

Table 3: Parameters of the nearest coordination shells around Cu atoms in Cu doped TiO_2-SiO_2. The number of nearest-neighbour atoms - N; distance (R), and Debye-Waller factors (σ^2). Uncertainty of the last digit is given in parentheses. A best fit is obtained with the amplitude reduction factor $S0_2 = 0.8$. The shift of the energy origin ΔE_o and the goodness of fit parameter, R-factor, are given in the last column.

4. Conclusions

We have developed a new low-temperature sol-gel synthesis of Cu modified TiO_2-SiO_2 photocatalysts, based on organic precursors. Colloidal solution of TiO_2-SiO_2 nanoparticles was prepared from titanium tetraisopropoxide, tetraethyl ortosilicate, and copper acetylacetonate as a source of Ti, Si and Cu, respectively. Photocatalytic measurements showed that the catalytic activity of TiO_2-SiO_2 is enhanced for a factor of 10 when 0.1 mol% of Cu is added to the TiO_2-SiO_2 matrix. All samples exhibited predominantly nanocrystalline anatase crystal structure of TiO_2 with a smaller amount of brookite phase, with the same crystal unit cell parameters and same crystal sizes independent of the relative amount of Cu in the TiO_2-SiO_2 matrix. No additional crystalline phases are present in the samples. SiO_2 is in the form of glass-like amorphous silicate nanoparticles. Cu K-edge XANES and EXAFS results show that the photocatalytic activity enhancement in TS_0.1Cu_150 sample is due to Cu^{2+} cations attachment on the surface of photocatalytically active TiO_2 nanoparticles. At higher Cu loadings, Cu-O-Ti connections are lost and Cu-O-Cu dimers are formed after drying at 150 °C, and consequently the photocatalytic activity of the material is hindered. Calcination of Cu modified TiO_2-SiO_2 photocatalysts at 500 °C induces significant structural changes: Cu-O-Ti connections are lost, Cu partially incorporates into the SiO_2 matrix, and amorphous copper oxides are formed, which again reduces the photocatalytic activity of the material. The results are crucial for the guidance of synthesis protocols in order to obtain more effective catalysts.

References

[1] A. Fujishima, T.N. Rao, D.A. Tryk, Titanium dioxide photocatalysis, J. Photochem. Photobiol. C Photochem. Rev. 1 (2000)

[2] K. Guan, Relationship between photocatalytic activity, hydrophilicity and self-cleaning effect of TiO2/SiO2 films, Surface and Coatings Technology (2005) 155−160]

[3] A. Soklic, M. Tasbihi, M. Kete, U. Lavrencic-Stangar, Deposition and possible influence of a self-cleaning thin TiO2/SiO2 film on a photovoltaic module efficiency, Catalysis Today 252 (2015) 54−60

[4] W. Choi, A. Termin, M.R. Hoffmann, Role of Metal-Ion Dopants in Quantum-Sized TiO2 âĂŞ Correlation between Photoreactivity and Charge-Carrier Recombination DynamicsJ. Phys. Chem. 98 (1994) 13669−13679

[5] B. Choudhury, M. Dey, A. Choudhury, Defect generation, d-d transition, and band gap reduction in Cu-doped TiO2 nanoparticles, Int. Nano Lett. 3 (2013)

[6] S. Klosek, D. Raftery, Visible light driven V-doped TiO2 photocatalyst and its photooxidation of ethanol, J. Phys. Chem. B. 105 (2002) 2815−2819.

[7] K. Su, Z. Ai, L. Zhang, Efficient Visible Light-Driven Photocatalytic Degradation of Pentachlorophenol with Bi2O3/TiO2−xBx, J. Phys. Chem. C. 116 (2012) 17118−17123.

[8] B. Xin, L. Jing, Z. Ren, B. Wang, H. Fu, Effects of Simultaneously Doped and Deposited Ag on the Photocatalytic Activity and Surface States of TiO2, J. Phys. Chem. B 109 (7) (2005) 2805−2809

[9] R. Chand, E. Obuchi, K. Katoh, H. N. Luitel, K. Nakano, Enhanced photocatalytic activity of TiO2/SiO2 by the influence of Cu-doping under reducing calcination atmosphere, Catalysis Communications 13 (2011) 49−53

[10] U. Cernigoj, M. Kete, U. Lavrencic-Stangar, Development of a fluorescence-based method for evaluation of self-cleaning properties of photocatalytic layers, Catalysis Today 151 (2010) 46−52

[11] S. Brunauer, P.H. Emmett, E. Teller, Adsorption of gases in multimolecular layers, J. Am. Chem. Soc. 60 (1938) 309−319

[12] K.S.W. Sing, D.H. Everett, R.A.W. Haul, L. Moscou, R.A. Pierotti, J. Rouquerol, Reporting physisorption data for gas/solid systems with special reference to the determination of surface area and porosity, Pure Appl. Chem. 57 (1985) 603−619

[13] E.P. Barrett, L.G. Joyner, P.P. Halenda, The determination of pore volume and area distributions in porous substances. I. computations from nitrogen isotherms, J. Am. Chem. Soc. 73 (1951) 373−380

[14] Ravel, B.; Newville, M. ATHENA, ARTEMIS, HEPHAESTUS: data analysis for X-ray absorption spectroscopy using IFEFFIT. J. Synchrotron Radiat. 2005, 12 (Pt 4), 537−541

[15] J. J. Rehr, R. C. Albers, S. I. Zabinsky, High-order multiple-scattering calculations of x-ray-absorption fine structure, Phys. Rev. Lett. 1992, 69, 3397−3400

[16] Wong, J., Lytle, F.W., Messmer, R.P., Maylotte, K-edge absorption spectra of selected vanadium compounds, D.H. (1984). Phys. Rev. B 30. 5596−5610.

Highly Sensitive Determination of Pyoverdine in Cloudwater by High-Performance Liquid Chromatography-Thermal Lens Spectrometry

L. Goljat

University of Nova Gorica, Vipavska 13, SI-5000 Nova Gorica

Abstract

Direct analysis of pyoverdine and Fe(III)-pyoverdine in cloudwater is reported for the first time. A newly developed high-performance liquid chromatography (HPLC) on reverse-phase (RP) C18 support coupled with thermal lens spectrometric detection (TLS), based on excitation at 407 nm by an krypton laser was used for this purpose. This HPLC-TLS method enabled a baseline separation of two structural isomers pyoverdine and two isomers of Fe(III)-pyoverdine in isocratic mode in less than 20 min. The novel HPLC-TLS method enabled separation and detection of pyoverdine and Fe(III)-pyoverdine with a single measurement. For both components the calibration curves were constructed in concentration range 5-30 μg/mL. The achieved limits of detection (LOD) in the HPLC-TLS system for Fe(III)-pyoverdine were 0.002 μg/mL which is 13 times lower than in the conventional HPLC-DAD system. LOD in the HPLC-TLS for pyoverdine were 15 ng/mL which is about 12 times lower than in an HPLC-DAD system, and about 4 times higher than in the HPLC-FLD system. The new method was applied on real cloudwater samples, sampled at Puy de Dôme Station (48^oN, 2^oE; 1465 m a.s.l.), in the Central Massif Region (Central France).

Keywords: cloudwater, pyoverdine, Fe(III)-pyoverdine, thermal lens spectroscopy, flow injection analysis, high-performance liquid chromatography

Email address: `leja.goljat@ung.si` (L. Goljat)

1. Introduction

A cloud is an aerosol comprising, a visible mass of liquid droplets, or frozen crystals, which are both made of water or various chemicals. The droplets or particles are suspended in the atmosphere above the surface of a planetary body. On the Earth clouds are formed by the saturation of air in the homosphere (troposphere, stratosphere and mesosphere) when air cools or gains water vapor [1]. The cloud system is a medium in which chemical species from the gas, solid, and aqueous phases are transformed. It plays a major role in the transformation of atmospheric compounds and influence the composition of atmosphere through liquid-gas exchanges [2]. Cloudwater is a complex mixture of organic and inorganic compounds, which originate from both the gas and the solid phases of the atmosphere. Organic species in the atmosphere e.g. formate, acetate and formaldehyde, originate from direct sources, such as automobile exhaust or are produced within the atmosphere by oxidation of hydrocarbons [3]. The dissolved organic matter is able to interact directly or indirectly with the aqueous chemistry of radicals, radical anions, nonradical oxidants, and transition metal ions, such as iron. Dissolved trace metals are also involved in different chemical processes in liquid atmospheric phase; they form complexes with water, ammonia, sulphate and therefore they play a significant role in the redox cycles of sulfur [4] and organic compounds [5]. Trace metals are usually introduced into the atmospere as a soil dust, fly ash from power plants, exhaust from combustion engines and from industrial operations [6]. In the past, cloud chemistry models have been developed, that considered microphysical and chemical interactions between different phases and chemical substances. Cloud chemistry models consider both detailed inorganic and organic mechanisms, and chemical transformations are mostly driven by radical pathways that define the cloud oxidant capacity. Oxidants, superoxide radical anion/hydro-peroxide radical couple, hydrogen peroxide and iron are crucial compounds because they initiate the chemical conversion of various substances through their oxidation [7]. Cloudwater also hosts microbial populations that are mainly biological aerosols and the dominant living aerosols that are present in the atmosphere. They can be integrated into the clouds because they can serve as cloud condensation nuclei for droplet formation [8]. The environment is stressful for airborne microorganisms, due to the low temperature, oxidation, UV radiation, acidic pH, etc. [8]. Within cloud water, microorganisms are metabolically active and, thus, are expected to contribute to the atmospheric chemistry; first, they could directly metabolize organic carbon species, and second,

2

they could reduce the available source of radicals through their oxidative metabolism. Consequently, molecules like hidrogen peroxide would no longer be available for photochemical or other chemical reactions, which would decrease the cloud oxidant capacity [9]. Some of microbial strains which were isolated from cloud water at the puy de Dome are *Pseudomonas* strains, *Sphingomonas* strain and yeast strain, and the contribution of microbial activity to carbon chemistry in clouds has been studied [11].

Flourescent *Pseudomonas* pecies produce, under certain conditions, yellow-green, fluorescent, water-soluble Fe(III)-chelating siderophores called pyoverdins and are present in the cloudwater [8]. The pyoverdins have a following common feature: a constant quinolone chromophore, responsible for color of the molecule, is bound to a peptide chain a dicarboxylic acid or to a dicarboxylic amide. Pyoverdine is the most important compound in iron metabolism and is structurally similar to pseudobactin. Since *Pseudomonas* species, which produce pyoverdine, are present in the cloudwater, hypothesis has been made, that the strong undefined ligands for iron, might be siderophores, produced by Pseudomona. High selectivity and sensitivity are required to detect pyoverdine, which is a powerfull chelator for Fe(III), with an affinity constant for this cation of about 10^{32} [12] and its Fe(III)-complex in cloudwater and to distinguish them. Until now, several techniques were applied for pyoverdine and/or Fe(III)-pyoverdine complex determination e.g. isoelectric focusing electrophoresis, spectrophotometry, ion chromatography (IC), UV-Vis spectrophotometry [12] and HPLC [13]. Some of them however lack of selectivity and sensitivity for detection of pyoverdine and its brown-red nonefluorescent complex Fe(III)-pyoverdine which is the most common form of the pigment in the nature and cannot be detected by sensitive detection of fluorescence. The pre-treatment of the sample would be neccessary to obtain a free pyoverdine, which could be analyzed by FLD. A highly sensitive spectrometric method thermal lens spectrometry (TLS) which can be easily coupled to separation techniques such as IC and HPLC or flow injection analysis including microunit chemical operations in microfluidic flows offers new possibilities for determination of pyoverdine in microliter samples, such as required for analysis of cloud water, which were investigated in this work.

2. 2. Materials and methods

2.1. Study area

Experimental studies were carried out at the at Puy de Dôme mountain (48°N, 2°E; 1465 m a.s.l.), in the Central Massif Region (Central France). It

is a strategic point from which warm and mixed clouds are present 50% of time between November and March. Clouds are frequently formed at the top of the site either during advection of frontal systems or by orographic rise of moist air. During winter/spring time, air masses are usually exempt from the influence of local pollution.

2.2. Sampling

Three cloud events were sampled in March 2016 at Puy de Dôme mountain (48°N, 2°E; 1465 m a.s.l.) (1.465 m above sea level). The cloud droplet sampling was carried out by a one stage cloud impactor with a protection screen for the wind; with aur flux used (86 m^{3}h^{-1}-) the lower limit of the aerodynamic diameter was about 7μm, which ensures 80% of collection efficiency. The impactor used in this work was made of stainless steel and aluminium. The samplimg time ranged from 40 to 120 minutes, depending on the liquid water content of the cloud. The fraction of samples for pyoverdine analysis was kept in the fridge at 4°C, and performed a week after collection. At every stage, sampling and analyses were carried out with the greatest precaution to minimise all possible contamination. To check data quality, we analysed two field blanks for each cloud event. Three cloud types were selected for their contrasting features: cloud 1 had a northwestern marine origin, cloud 2 was from the continental southwest, and cloud 3 was from the continental northeastern flux but was influenced by anthropogenic emissions. The average temperatures during sampling were 10°C for clouds 1 and 3 and 13.5°C for cloud 2.

2.3. Chemicals and standards

HPLC gradient grade methanol (MeOH) and citric acid (C$_6$H$_8$O$_7$) were purchased from Sigma-Aldrich (Steinheim, Germany). Ammonium acetate (NH$_4$OAc) was purchased from Kemika. Iron(III) chloride was purchased from Alfa Aeser. Double deionized water was used. Standards were stored at 4°C. Pyoverdine standards were prepared as follows: an accurately weighed amount of pyoverdine standard was dissolved in an appropriate volume of water in order to gain 280 μg/mL solution, subsequently dilutions until 30 g/mL concentration were made using water or mixture of MeOH:H$_2$O (1:9). The final standard solutions, as well as sample solutions, were prepared on a daily bases and were not filtered in order to prevent the loss of pyoverdine. Pyoverdine-Fe(III) standards were prepared as follows: an accurately weighed amount of pyoverdine standard was dissolved in an appropriate volume of water in order to gain 280 μg/mL solution, and an accurately weighed amout of FeCl$_3$ was dissolved in appropriate volume

4

of water in order to gain 98 μg/mL solution. Subsequently dilutions until 30 μg/mL concentration were made by adding different volumes of pyoverdine standard solution and 100 μL of $FeCl_3$ standard solution, using water or mixture of MeOH:H_2O (1:9) to dilute. The final standard solutions, as well as sample solutions, were prepared on a daily bases and were not filtered in order to prevent the loss of pyoverdine.

2.4. HPLC-DAD analyses

HPLC-DAD analyses were conducted using the commercial Agilent 1100 Series system (Agilent Technologies, Waldbronn, Germany), consisting of a quaternary pump (G1311A QUAT PUMP), degasser (G1322A), thermostated autosampler (G1313A ALS) with a 20 μL injection loop and a diode-array detector (G1315A DAD). ChemStation (for LC 3D system Rev. B01.03 204, Agilent Technologies 2001-2005) was used for evaluation of the collected data. In each run 20 μL of each solution was injected. Flow rate was set to 0.6 mL/min and column temperature was adjusted to 40°C and the acquisition wavelength was set to 407 nm to match the excitation wavelength available from kripton laser (407 nm) in TLS experiments, which is close to the absorption maximum of pyoverdine-Fe(III) (403 nm) complex and pyoverdine (385 nm). The mobile phases used for BR analysis consisted of MeOH: 20 mM NH_4OAc (95:5, v/v) with a run time of 25 min. Separations were performed on a stainless steel BDS Hypersil C18 column (100 mm x 4.6 mm I.D.) and pre-column (4.0 mm x 4.6 mm I.D.) with a particle size of 3μm and pore size of 120 (Thermo Fisher Scientific, Waltham, USA).

2.5. HPLC-TLS analyses

HPLC-TLS analyses were performed using a HPLC pump (Knauer Smartline Pump 1000, Berlin, Germany), manual injector (Rheodyne, Model 7725) 8 μL flow-through detection cell with 1 cm optical path length and a dual-beam TLS detection unit [Fig. 1]. In each run 20 μL of each standard solution was injected manually while other chromatographic conditions were as stated in Section 2.4. Pyoverdine determination was accomplished using a dual-beam, mode-mismatched thermal lens spectrometer. The excitation beam originating from a krypton laser, tuned to 407 nm providing 110 mW of power was modulated by a mechanical chopper (Scitec Instruments, Redruth, Cornwall, UK) at 26 Hz, and was focused onto a sample cell by a 70 mm focal length lens (Edmund Optics, Barrington, NJ, USA). Two additional lenses (Edmund Optics), first with 100 mm and second with 70 mm of focal length, were added before the sample cell to focus He-Ne laser
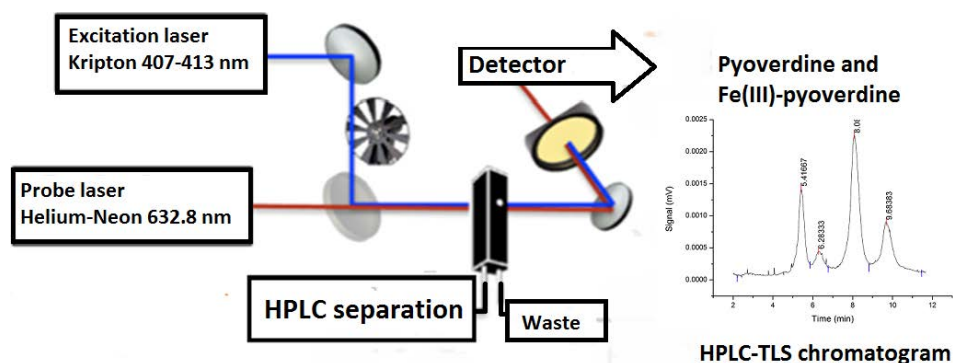
Figure 1: Schematic presentation of HPLC-TLS system

(Melles Griot, Uniphase 1103P; Fremont, CA, USA), probe beam at 632.8 nm with 2 mW of power. The confocal distance of the probe beam was 5.56 mm. The ratio of the probe beam to the excitation beam diameters in the sample cell was 3.5. The changes in the probe-beam intensitiy after passing the flow-through path of the cell and through an optical filter for the removal of the excitation beam, were monitored behind a pinhole by a pin photodiode equipped with an interference filter (Melles Griot) and connected to a lock-in amplifier (Stanford Research Instruments, model SR830 DSP, Sunnyvale, CA, USA), which amplified only the component of the input signal that appears with the frequency of the reference signal from the modulator. This was achieved by a Fourier transformation of the signal while filtering out all other frequencies with a low-pass filter. The lock in amplifier was connected to a computer, where the data were collected using the Matlab programme. The value od the modulation frequency provided maximal signal to noise ratio (S/N) in a frequency range accessible by collinear propagation of the excitation beam and the probe beam through the flow-through cell, which was located at the focal point of the excitation beam beyond the probe beam wast. Its optimal position, with respect to the focus of the probe beam, was determined experimentally. The beam excitation powers were measured at the location before the flow-through detection cell. Two isomers of pyoverdine and two isomers of Fe(III)-pyoverdine were separeted on Hypersil gold chromatograhic column and detected by TLS spectrometer, based on excitation at 407 nm by a krypton laser. The separation was performed in an isocratic mode. The detection was performed in a 1 cm flow-through sample cell.

6

3. Results and discussion

Pyoverdine occurs in biological samples and in standards in the form of two different structural isomers and two forms of Fe(III)-pyoverdine isomers. The HPLC conditions were varied in order to obtain the best resolution of isomers together with the tendency to have the maximum amount of organic solvents and minimal amount of water in the mobile phase, required to obtain the maximal thermal lens effect (mobile phase in our case), namely temperature coefficient of refractive index and thermal conductivity, also have an impact on the magnitude of the thermal lens effect [14]. Therefore, the composition of the mobile phase was chosen in order to maximize $\delta n/\delta T$ and minimize k. As a result of testing different HPLC columns, C18 BDS Hypersil gold column with carbon load of 11%, 3 mm i.d., 150 mm length and 3 micron particle size was chosen. The column enabled the best resolution for separated isomers with adequate retention times while using a relatively low water content in the mobile phase. The addition of NH_4OAc into mobile phase to provide NH^{4+} as a counter ion to pyoverdin was obligatory, as otherwise pyoverdine was not retained in the column.

Measurements of fluorescence of the free pyoverdine solution, characterized by its yellow-green colour and strong fluorescence, reveaed two peaks, pyoverdine A and pyoverdine B [Fig. 2]. The ratio, which was calculated from peak areas, is pyoverdine A:pyoverdine B=1:2.7. HPLC-DAD method revealed four major peaks; pyoverdine A, Fe(III)-pyoverdine A, pyoverdine B, Fe(III)-pyoverdine B [Fig. 2]. These peaks reavealed that also some Fe(III)-complex is present in the solution. The absorption spectrums of all four peaks were obtained by DAD.The absorption spectrums of pyoverdine A and pyoverdine B in water were similar and showed two main bands at pH=7: one at 230 nm with a shoulder at 255 nm and the other at 400 nm [Fig. 3], which match the absorption spectrum of pyoverdine previously reported [12]. Addition of an aqueous solution of $FeCl_3$ to the pyoverdine aqueous solution caused immediate colour change to brown-red accompained by a total disappearance of fluorescence. HPLC-DAD method revealed two peaks; Fe(III)-pyoverdine A and Fe(III)-pyoverdine B [Fig. 4]. The ratio, which was calculated from peak areas, is Fe(III)-pyoverdine A:Fe(III)-pyoverdine B=1:2.4. These peaks reavealed that also some Fe(III)-complex is present in the solution. The absorption spectrums of all four peaks were obtained by DAD. The absorption spectrums of Fe(III)-pyoverdine A and Fe(III)-pyoverdine B in water were similar and showed two main bands at pH=7: one at 235 nm with a shoulder at 265 nm and the

other at 403 nm with a shoulder at 450 nm [Fig. 6], which match the absorption spectrum of pyoverdine previously reported [12]. Chromatograms obtained by HPLC-TLS [Fig. 7 and 8] demonstrate that the HPLC-TLS method is sensitive and sufficiently selective for precise and accurate pyoverdine and Fe(III)-pyoverdine determination. On the basis of calibration curves the limits of detection (LOD) of this technique were calculated by the formula:

$$LOD=3SD_{blank}/slope_{cal.curve}$$

Where SD_{blank} is the standard deviation of blank signal and $slope_{cal.curve}$ is the slope od calibration curve.

Accordingly the achieved limit of detection (LOD) in the HPLC-TLS system for Fe(III)-pyoverdine was 0.002 μg/mL which is 13 times lower than in the conventional HPLC-DAD system (LOD=0.028 μg/mL). LOD in the HPLC-TLS for pyoverdine was 15 ng/mL which is about 12 times lower than in an HPLC-DAD system (LOD=0.174 μg/mL), and about 4 times higher than in the HPLC-FLD system (LOD=0.004 μg/mL). For both components the calibration curves were constructed with linear response in concentration range 5-30 μg/mL . The novel isocratic RP-C18 HPLC-TLS method enables separation and determination of pyoverdine and Fe(III)-pyoverdine in a single run and excels in superior sensitivities when compared to conventional HPLC-DAD system. The developed method was applied on real cloudwater samples, sampled at the Puy de Dome Station.

4. Conclusions

The novel HPLC-TLS method enabled separation and detection of pyoverdine and Fe(III)-pyoverdine with a single measurement. This is the first report of a direct measurement of Fe(III)-pyoverdine concentration in cloudwater without sample pre-concentration or other preparation. Although the HPLC-DAD method, developed here for the sake of comparison with the HPLC-TLS method, outperforms the existing methods in terms of sensitivity, direct assessment of free Fe(III)-pyoverdine was enabled only when a TLS detector was used. The study revealed that Fe(III)-pyoverdine concentrations in cloudwater are around 0.013 μg/mL, which is in the range of previously reported values obtained either theoretically or experimentally. The experiment has confirmed hypotesis that metabolically active microorganisms, which are present in the cloudwater [9] produce yellow-green, fluorescent, water-soluble Fe(III)-chelating siderophores

called pyoverdins, which were detected in all three real samples. This means that we could also investigate the presence of this microorganism in cloudwater by simple and rapid detection od Fe(III)-pyoverdine.

References

1. "Weather Terms". National Weather Service. Retrieved 21 June 2013.

2. Jacob, D. J. 1986. Chemistry of OH in remote clouds and its role in the production of formic acid and peroxymonosulfate. J. Geophys. Res. 91:98079826.

3. Fuzzi, S., M. C. Facchini, S. Decesari, E. Matta, and M. Mircea. 2002. Soluble organic compounds in fog and cloud droplets: what have we learned over the past few years? Atmos. Res. 64:8998.

4. Jacob, D.J., Hoffman, M.R.: A dynamic model for the production of H+, NO3- and SO42- in urban fog. J. Geophys. Res. 88, 6611-6621, 1983

5. Zuo, Y., and Hoigne, J.: Formation of hydrogen peroxide and depletion of oxalic acid in atmospheric water by photolysis of iron (III)-oxalato compounds, Envir. Sci. Technol., 26, 1014-1022, 1992

6. Hoffman, M.R., Jacob, D.J.: Kinetics and mechanisms of the catalytic oxidation of dissolved sulphur dioxide in aqueous solution: An application to nighttime fog water chemistry, In Calvert, J.G. (ed). SO2, NO and NO2 Oxidation Mechanisms: Atmospheric Considerations. Butterworth Publishers, Boston, MA, pp.101-172, 1984

7. Charbouillot, T., Gorini, S., Voyard, G., Parazols, M., Brigante, M., Deguillaume, L., Delort, A.- M., and Mailhot, G.: Mechanism of carboxylic acid photooxidation in atmospheric aqueous 30 phase: formation, fate and reactivity, Atmos. Environ., 56, 18, 2012.

8. Delort A-M, et al. (2010) A short overview of the microbial population in clouds: Potential roles in atmospheric chemistry and nucleation processes. Atmos Res 98(24):249260.

9. Vatilingom, M., Deguillaume, L., Vinatier, V., Sancelme, M., Amato, P., Chaumerliac, N., Delort, A.-M., 2013. Potential impact of microbial activity on the oxidant capacity and organic carbon budget in clouds. Proc. Natl. Acad. Sci. 110, 559564. doi:10.1073/pnas.1205743110

10. Hill, K. A., P. B. Shepson, E. S. Galdavy, C. Anastasio, P. S. Kourtev, A.Konopka, and B. H. Stirm. 2007. Processing of atmospheric nitrogen by clouds above forest environment. J. Geophys. Res. 112:D11301. doi:1029/ 2006JD008002

11. Vatilingom, M., Deguillaume, L., Amato, P., Sancelme, M., Amato,

P., Laj, P., Leriche M., Delort, A.-M., 2013. Contribution of Microbial Activity to Carbon Chemistry in Clouds.. Applied and environmental microbiology, jan. 2010, p. 2329

12. Meyer J. M., Abdallah M. A., 1978. The Fluorescent Pigment of Pseudomonas fluorescens : Biosynthesis, Purification and Physicochemical Properties. Journal of General Microbiology 107, 319-328. Great Britain

13. Bultreys A., Gheysen I., Wathelet B., Maraite H. and Edmond de Hoffmann E., High-Performance Liquid Chromatography Analyses of Pyoverdin Siderophores Differentiate among Phytopathogenic Fluorescent Pseudomonas SpeciesApplied and environmental microbiology, feb. 2003, p. 11431153.
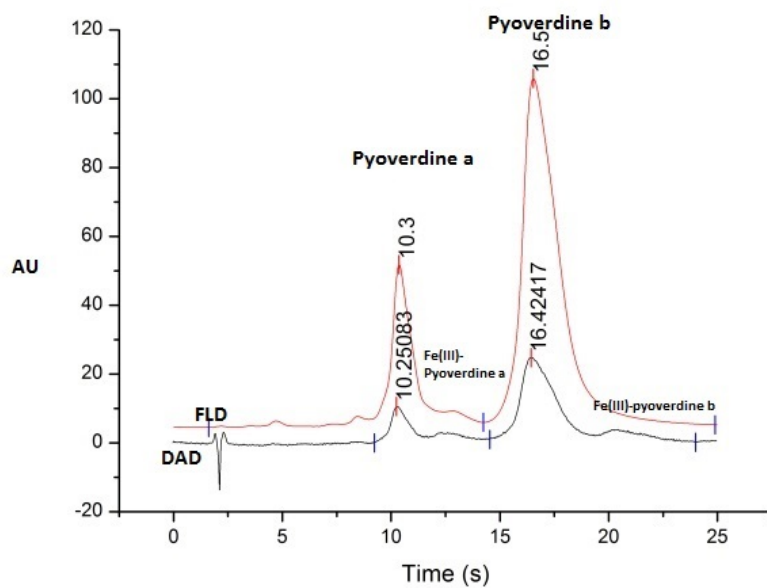
Figure 2: Pyoverdine chromatogram by HPLC-DAD and HPLC-FLD
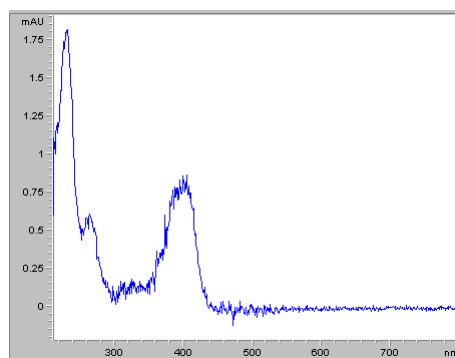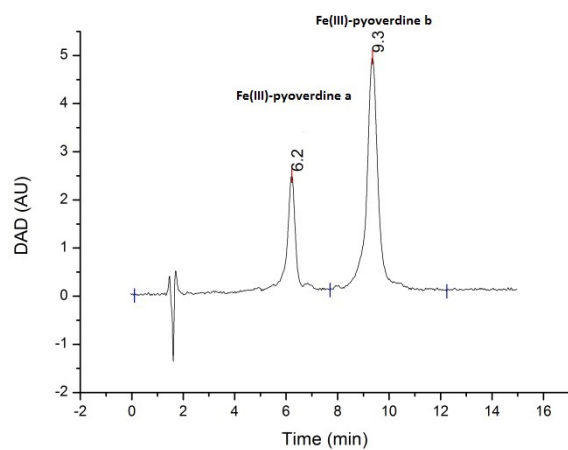

Figure 3: Absorption spectrum of free pyoverdine

11

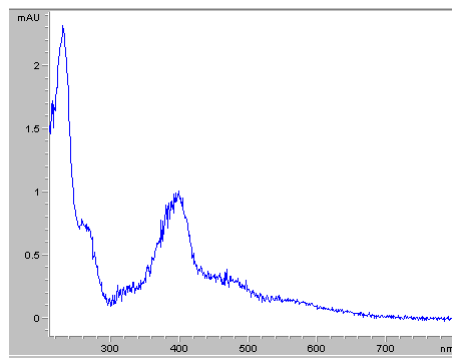Figure 4: Fe(III)-pyoverdine chromatogram by HPLC-DAD

Figure 5: Fe(III)-pyoverdine absorption spectrum

Temperature controlled polycarbosilane de-agglomeraton

Andraž Mavrič

University of Nova Gorica, Vipavska 13, SI-5000 Nova Gorica

Abstract

Use of polycarbosilane macromolecules, where morphology on nanoscale should be precisely controlled, has been hindered by not understanding proper molecular size and solubility conditions. In the case of polycarbosilanes solutions, finding the appropriate solvent and solubility conditions has been a challenge, due to a fact that, as a result of strong inter- and intra-molecular attractions, agglomeration and successive precipitation take place even at very low polymer concentrations. Insufficient understanding of the polymer state in the solution prevented accurate determination of molecular weight and size. We manage to achieve a control over the particle size of three topologically different polycarbosilanes. We showed that at room temperature the agglomerates in a range of 600 - 1300 nm are present and are precipitating with time. With just a slight temperature increase to above 40 °C the agglomerates undergo decomposition to the dispersed particles with the size in a range from 15 to 45 nm. The de-agglomeration process was followed with a Dynamic Light Scattering (DLS) and has very similar characteristics for polycarbosilanes of the three different topologies. The decomposition of agglomerates and the transition to a single phase system was studied with an isothermal Differential Scanning Calorimetry (DSC) and a Thermogravimetric Analysis (TGA).

Keywords: polycarbosilane, dynamic light scattering, polymer size, de-agglomeration

1. Introduction

Polycabosilanes are polymeric molecules consisting of Si atoms in the skeleton, they are promising materials for many technological applications. First they were recognized as preceramic precursors to silicon carbide fibers [1]; later they have been applied as potential semiconductors [2], photoconductors [3] and resists in UV lithography [4, 5]. Technological applications, especially on nanoscale, where synthesis and deposition originates from solution, are strongly hindered by the polysilane solubility due to strong intermolecular interactions. Recent knowledge in applying macromolecules in nanotechnologies revels the importance of understanding polymer state in a solution. For instance, the attraction between macromolecules defines the characteristic of a thin film (film roughness, thickens, interconnectivity of macromolecules) and directly affects a charge transfer in semiconductive polymers [6, 7], in lithography line-edge roughness and resolution are affected by the polymer agglomeration [8]; a thickness of hard coatings based on polysilane is limited by polymer aggregate size [9]; a size of SiC nanoparticles depends on dispersion of molecules in precursor solution [10]. These technological problems originate in an insufficient understanding of size distribution of the polysilane molecules and their dispersion in different solvents.

For the study of size distribution and dispersion in solution polymethysilane (PMSy) was selected, because its size can be controlled already during synthesis. PMSy is a polymer that can be synthesized electrochemically from trichloromethylsilane [11], a monomer that can branch in three directions and form a trifunctional starburst dendrimer. During the growth of dendrimer like polymers the volume occupied by the polymer grows exponentially with the number of generations on the other hand accessible volume only grows cubically, as a result the polymer reaches a generation where maximal density is achieved and the growth stops [12], therefore there is a finite size that polymer can achieve.

The most of the results have been reported in terms of molecular weight, although this is not a directly measurable quantity, both light scattering and gel chromatographic techniques measure quantities related to a hydrodynamic diameter, which is later converted to the molecular weight [13]. The conversion depends on a size scaling regime of polymer solutions and can lead to a discrepancy between the light scattering and gel chromatography data [14]. It is known that the molecular weights obtained by gel permeation chromatography with polystyrene standard should be used only relatively, as the polystyrene standard used was not found to be a good model

for polysilanes. The light scattering was suggested as a reliable method, but until now the problems with solution conditions, that will give reliable data has not been solved. The measurements of the polymer molecule size become strongly dependent on the polymer solubility and the conditions within the mixing phase diagram. In addition, these techniques cannot differentiate between the de-agglomerated and agglomerated particles. This explains the wide span of polysilane sizes, from 200 nm to 2 μm, reported in the literature [15, 16].

In this study we manage to control particle size of polymethilsilane and two other topologically different polycarbosilanes. We showed that at room temperature agglomerates in range of 600 - 1300 nm are present. With just slight temperature change above 40 °C the agglomerates undergo decomposition and particles in range from 15 to 45 nm were found. The de-agglomeration process was followed by the Dynamic Light Scattering (DLS) and Differential Scanning Calorimetry (DSC) measurements. We show that this process has very similar characteristics for polysilanes of all three different topologies. We report a typical molecular size of three types of polymers in the nanoscale. The reported knowledge on temperature control of polycarbosilane molecule/aggregate sizes in solution will open a new approach in applying polycarbosilanes in nanotechnology.

2. Materials and methods

Polymethylsilyne (PMSy) was synthesized using the electrochemical method. The entire synthesis process was conducted in a dry box. In a mixture of 12 mL of acetonitrile[1] and 3 mL of methyltrichlorolsilane monomer, CH_3SiCl_3[2], 0.5 g of anhydrous $AlCl_3$[3] was dissolved. The solution was placed in an electrochemical cell with two aluminum electrodes and left stirring for 15 minutes. A potential of 5.5 V was applied with a power supply PS3020[4] until the current dropped to 99 % of the initial current, which assured that the polymerization was completed. The synthesized product was end-capped with 1 mL of 2.0 M $LiAlH_4$ in tetrahydrofuran[5] (THF) and left stirring overnight to remove residual chlorine from the polysilane. The

---

[1] J.T.Baker, Phillipsburg, NJ
[2] Alfa Aesar, Karlsruhe, Germany
[3] Aldrich, Steinheim, Germany
[4] HQ Power, Gavere, Belgium
[5] Aldrich, Steinheim, Germany

product was cleaned with extraction in n-pentane[6] to remove salts. After evaporation of pentane a yellow viscous oil/paste was obtained with a yield of around 50 %. For studyng of electrochemical processes the reference electrode (Pt wire) was introduced between two aluminium electrodes and the potential between working aluminium chatode and reference electrode was monitored by the potentiostat ZIVE SP1[7] in open circuit mode. The electrolysis was done on a mixture of 12mL of acetonitrile and 3 mL of methyltrichlorosilane monomer using 0.5 g of $AlCl_3$ or 0.1 M tetrabutilamoniumtetrafluoroborate (TBATF) as an electrolyte. The electrolysis proceeded in constant current mode with 500 mA or 200 mA current applied between aluminium electrodes.

Commercially available poly(dimethylsilane)[8] (PDMS) and polycarbosilane[9] (PCS) were used. The polymethylsilyne (PMSy, Fig. 1a) is a dendrimer, formed by each Si atom ideally bound to three other Si atoms and a methyl group [17, 16, 18]. Polycarbosilane (PCS, Fig. 1b) is a layered network where the Si atoms are bound to other Si over bridging C atoms [19]. Polydimethylsilane (PDMS, Fig. 1c) is a linear polymer with Si atoms in the chain [20, 21].
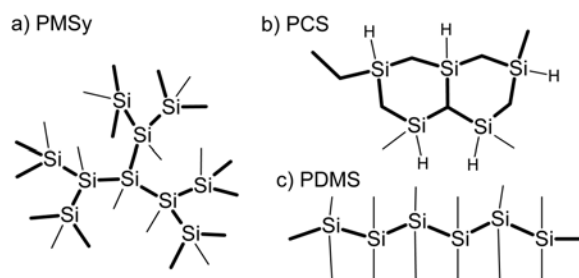

Figure 1: Schematic presentation of structural units of the three polycarbosilane structures with different topologies; a) dendrimer [17, 16, 18], b) network [19] and c) chain [20, 21].

The polymer solutions were prepared in extra dry THF[10] or absolute anhydrous ethanol[11]. Concentrations for DLS measurements (2.5 mg/mL for PMSy, 0.05 mg/mL for PDMS and 50 mg/mL for PCS) were kept as low as

---

[6] Alfa Aesar, Karlsruhe, Germany

[7] WonATech, Seoul, Korea

[8] Aldrich, Steinheim, Germany

[9] Nabond Technologies Co., Ltd., Hong Kong

[10] Acros Organics, Geel, Belgium

[11] Carlo Erba, Val De Reuil, France

possible to stay in a dilute regime and just above the detection limit of the instrument. The solutions were treated in an ultrasound bath for 1 minute to degas and then left 30 minutes at room temperature to equilibrate before DLS measurements. The particle size measurements were preformed with a 90Plus/BI-MAS DLS system and data were processed with 9KPSDW software package[12]. The results were obtained as an average of 6 runs with duration of 5 minute. The temperature dependent particle size is given for 5 °C temperature steps with intermediate 1h equilibration.

The DSC analysis was conducted with a TGA/DSC 2 system[13] using nitrogen as a protective and inert gas and 70 μL platinum crucible covered with a lid with 50 μm hole. The isothermal DSC plots were recorded at 35, 36, 38, 40 and 45 °C.

3. Results

3.1. Synthesis of the Polymethylsilyne

To avoid the effect of solution resistance the electrolysis was done in constant current regime, the potential between two Al electrodes and between Al cathode and Pt reference electrode was recorded during the synthesis (Fig. 2). The potential vs. reference electrode drifts for around 0.3 V from beginning to the end of synthesis. The end is indicated by the rapid increase in the potential because the reaction mixture run out of monomer, the same trend is followed for the potential between both Al electrodes. The two Al electrodes are electrodes between which electrical current is flowing and the drift to higher potential during the time of the synthesis is a result of change in solution resistance The drift in potential vs. reference electrode is therefore due to increase of solution resistance and is practically constant during time of synthesis. Constant potential indicates that only one reaction is taking place at cathode, this is the reduction of Si-Cl bond on monomer to form dichlorometilsialne anion. The polymerization proceeded with addition of anion, the yield of passed charge for the reduction of a monomer to the anion is for synthesis at 500 mA and 200 mA, 90 % and 87 % respectively.

The reduction of Si-Cl bond to anion and formation of dimer agrees with literature that reports mechanism of dichloroorganosilane reduction [22,

---

[12]Brookhaven Instruments Corporation, Holtsville NY
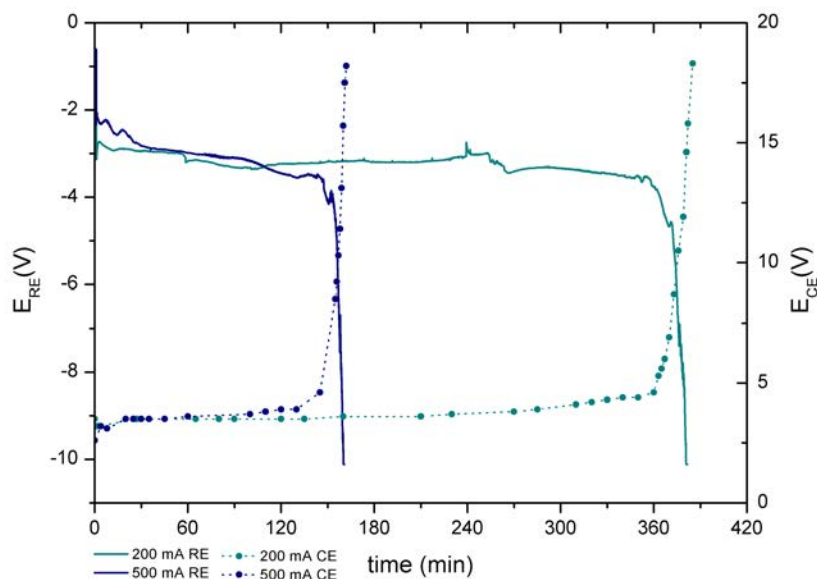[13]Mettler Toledo

Figure 2: The potential between working and reference electrode (RE) and counter and working electrode (CE) during the constant current electrolysis with TBATF electrolyte at 500 and 200 mA.

23, 24, 25, 26], but we disagree with mechanism proposed for polymerization of trichloroorganosilane proposed by [25, 26]. After the addition of anion and formation of dimer they propose reduction of Si-Cl bond on dimer and on higher oligomers to form network structure. Our results indicate that on electrode only monomer reduction to anion is possible, the reduction of higher oligomers will demand higher potential due to sterical hindrance. The steric effect for dichloroorganosilanes is demonstrated by exchanging a metil group for a sterically biger cyclohexil group, the reduction potential is already 0.9 V lower [22]. The mechanism of polymer growth from electrochemical reduction of trichlorometilsilane results in dendrimer and not in the network topology.

3.2. Dynamic light scattering

To determine the molecular size we carried out the time-dependent DLS measurements, measured diameter for three freshly prepared polymer solutions is shown on Fig. 3b, it remained approximately constant during 5-10 hours time. Time-dependent measurements of concentration in solution
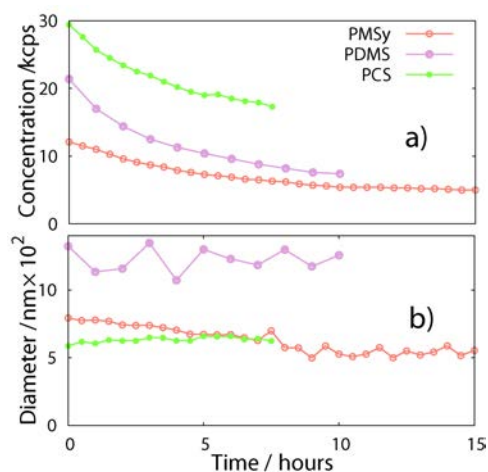
6

Figure 3: Time-dependent DLS measurements of PMSy, PDMS and PCS polymer solutions at 25 °C: a) concentration decreases with time exponentially; b) hydrodynamic diameter of the particles are constant during time of measurement. Concentration is given in kilo counts per second of detected scattering events (kcps) that depends linearly on concentration. After some time the signal disappears due to precipitation.

(shown on Fig. 3a, concentration given in kpcs, kilocounts per second, signal depends linearly on concentration) revealed the exponential decrease of concentration that droped below a detection limit of the instrument (~1 kcps) after several hours. After treating the samples with ultrasound, the signal for the concentration recovered back to the initial value. This indicates that the solutions are not stable at room temperature, decrease in concentration is connected with precipitation of agglomerates as they settle on the bottom of the cuvete they become invisible to the DLS laser beam. Because DLS only gives the signal from the particles that remain in the solution, the diameter stays constant until concentration decreases so low that signal vanished, at this point precipitation on the bottom of the cuvete is also visually observed.

To change the polymer-solvent interactions we performed the temperature-dependent DLS experiments. The results of these experiments (Fig. 4 left) show an abrupt drop in the average particle size of all three studied polymers in a temperature range from 25 to 50 °C. The heat-treated samples were cooled down to room temperature, mixed with ultrasound and measured with DLS. The obtained size distributions were similar to those of the freshly prepared sample, showing that size change was not due to chemical reactions. The drop induced by the increase in temperature is enormous:
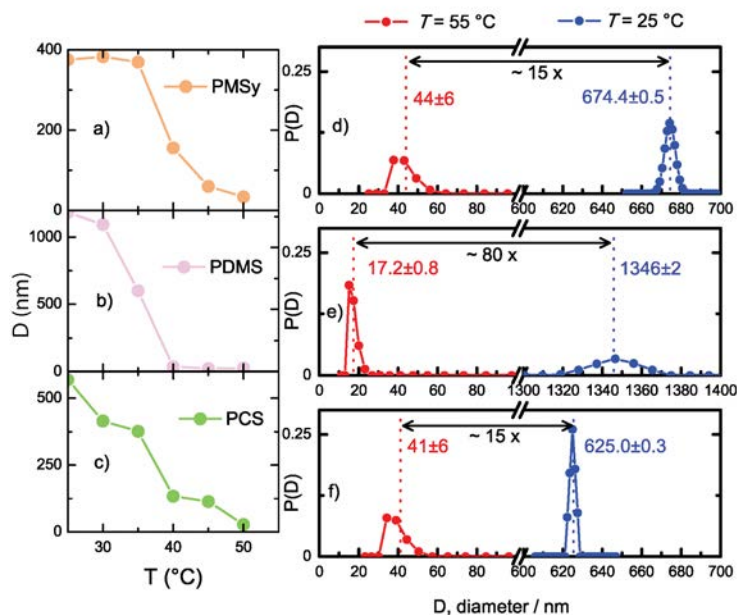
Figure 4: DLS measurements of a particle hydrodynamic diameter, D, for three polymer species. Left - temperature dependence of D for a) PMSy, b) PDMS and c) PCS. Right - particle size distributions, P(D), at 25 °C (blue) and 55 °C (red) for d) PMSy, e) PDMS and f) PCS after 5 hours of equilibration. Values and positions of the average diameters are shown with numbers and vertical dashed lines. The two-sided black arrows indicate a factor of change of average diameters, ranging from 15 up to 80 times.

about two orders of magnitude, from about 15 to 80 times as shown on the size distribution (Fig. 4 right).

3.3. Differential scanning calorimetry

We consider the drop in size as an indication that the system crossed the binodal on the Flory-Huggins phase diagram of mixing, where particles in solution and precipitate is present, and appeared in the single-phase regime of the solution. To confirm that the extensive conformational reordering is taking place, we also performed isothermal DSC and TGA kinetic studies (Fig. 5), within the same temperature range as at DLS analyses. The DSC/TGA curves indicated on a change in the solution state. At a low temperature of 35 °C, flat DSC and TGA lines were recorded.
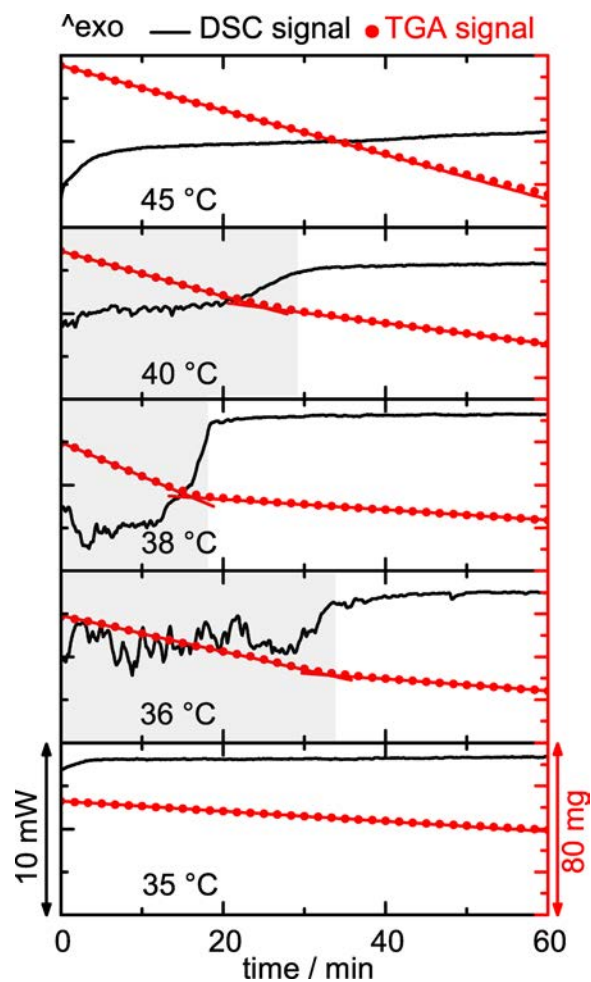
Figure 5: Isothermal DSC and TGA kinetic studies of PCS indicating structural changes within the temperature range from 36 to 40 °C. The area where structural changes are detected is shadowed.

At a temperature, just one degree higher (36 °C), multiple endothermic peaks appeared in the DSC signal indicating on the agglomeration/de-agglomeration processes typical for a metastability region. The presence of the multiple peaks on the DSC signal (and therefore the phase transition) is recorded in temperature range from 36 to 40 °C. An additional confirmation for the presence of the phase transition comes from a sudden change in a slope of the TGA curves, which indicates on a decrease in a solvent evaporation rate, as a consequence of an increase in a number of polymer

9

particles due to de-agglomeration, decrease in their sizes and increase in polymer-solvent interaction surface. At a higher temperature of 45 °C, the flat DSC and TGA lines were recorded again, indicating the absence of the phase transition due to the fact that the polymer molecules are already fully de-agglomerated.

4. Conclusions

An important step in determining molecular size is achieving proper solution properties. For three polycarbosilanes with different topologies we manage to drive the solution into the regime where it was stable and aggregates of molecules de-agglomerated by the increase in the temperature to around 40 °C. In this state we were able to determine molecular size (radii) to be around 20 nm. Because the interactions between solvent and polymer are independent of polymer topology and are rather related to chemical composition, the three topologically different polycarbosilanes showed the same behavior in the same temperature range. Through the understanding of the polycarbosilane molecular size and solubility conditions, this study opens the way for more reproducible and targeted application of the polycarbosilanes nanotechnology.

References

[1] S. Yajima, Y. Hasegawa, K. Okamura, T. Matsuzawa, *Development of high-tensile strength silicon-carbide fiber using an organosilicon polymer precursor*, Nature 1978, 273, (5663), 525-527.
[2] R. West, L. D. David, P. I. Djurovich, K. L. Stearley, K. S. V. Srinivasan, K. S. V., H. Yu, *Phenylmethylpolysilanes - formable silane copolymers with potential semiconducting properties*, J. Am. Chem. Soc. 1981, 103, (24), 7352-7354.
[3] R. G. Kepler, J. M. Zeigler, L. A. Harrah, S. R. Kurtz, *Photocarrier generation and transport in sigma-bonded polysilanes*, Phys. Rev. B 1987, 35, (6), 2818-2822.
[4] R.D. Miller, G. Wallraff, N. Clecak, R. Sooriyakumaran, J. Michl, T. Karatsu, A. J. McKinley, K. A. Klingensmith, J. Downing, *Polysilanes - photochemistry and deep-uv lithography*, Polym. Eng. Sci. 1989, 29, (13), 882-886.
[5] S. Hayase, *Polysilanes for semiconductor fabrication*, Prog. Polym. Sci. 2003, 28, (3), 359-381.
[6] B. Martin, *Structure and morphology control in thin films of regioregular poly(3-hexylthiophene)*, J. Polym. Sci. Part B: Polym. Phys. 2011, 49, (17), 1218-1233.

[7] K. Tremel, S. Ludwigs, *Morphology of P3HT in Thin Films in Relation to Optical and Electrical Properties. In P3HT Revisited From Molecular Scale to Solar Cell Devices*, Springer Berlin Heidelberg: 2014, 265, 39-82.

[8] Y. Toru, N. Hideo, N. Masao, K. Kenji, K. Yoshio, *Advances in Resist Technology and Processing XVI*, 1999, 3678, 617-624.

[9] M. Valant, U. Luin, M. Fanetti, A. Mavric, K. Vyshniakova, Z. Siketic, M. Kalin, *Fully transparent nanocomposite coating with an amorphous alumina matrix and exceptional wear and scratch resistance*, Adv. Funct. Mater., 2016, 26, (24), 4362-4369.

[10] M. Dragomir, M. Valant, M. Fanetti, Y. Mozharivskyj, *A facile chemical method for the synthesis of 3C-SiC nanoflakes*, Rsc Adv. 2016, 6, (26), 21795-21801.

[11] D. Eroglu, Y. Nur, U. Soenmez, G. Bayram, M. W. Pitcher, *Batteries and a Pinch of Salt: A Simple Toolkit for the Production of Poly(methylsilyne)*, J. Appl. Polym. Sci. 2009, 112 (6), 3519-3521.

[12] P. G. De Gennes, H. Hervet, *Statistics of "starburst" polymers*, J. de Phys.Lett. 1983, 44, (9), 351.

[13] M. Rubinstein, *Polymer Physics*, Oxford University Press, 2003

[14] R. West, *The polysilane high polymers*, J. Organomet. Chem. 1986, 300, (1-2), 327-346.

[15] R.D. Miller, J. Michl, *Polysilane high polymers*, Chem. Rev. 1989, 89, (6), 1359-1410.

[16] M. Okano, K. Nakamura, K. Yamada, N. Hosoda, M. Wakasa, *An improved electrochemical synthesis of network polysilanes*, Electrochemistry 2006, 12, 956-958.

[17] P. A. Bianconi, F. C. Schilling, T. W. Weidman, *Ultrasound-mediated reductive condensation synthesis of silicon-silicon-bonded network polymers*, Macromolecules 1989, 22, (4), 1697-1704.

[18] M. W. Pitcher, S. J. Joray, P. A. Bianconi, *Smooth continuous films of stoichiometric silicon carbide from poly(methylsilyne).*, Adv. Mater. 2004, 16, (8), 706.

[19] H. Q. Ly, R. Taylor, R. J. Day, F. Heatley, *Conversion of polycarbosilane (PCS) to SiC-based ceramic - Part 1. Characterisation of PCS and curing products.*, J. Mater. Sci. 2001, 36, (16), 4037-4043.

[20] C. A. Burkhard, *Polydimethylsilanes*, J. Am. Chem. Soc. 1949, 71, (3), 963-964.

[21] S. S. Bukalov, L. A. Leites, R. R. Aysin, I. S. Bushmarinov, A. O. Dmitrienko, A. A. Korlyukov, M. I. Buzin, V. S. Papkov, N. A. Chernyavskaya, A. I. Chernyavskii, *The structure and phase transitions of crystalline polydimethylsilane Me2Si(n) revisited*, Russ. Chem. Bull. 2014, 63, (11), 2515-2526.

[22] X. Wang, Y. Yuan, I. Cabasso, *Cyclic Voltammetric Study of Electroreduction of Dichlorosilanes*, Electrochem. Soc. 2005, 152, E259.

[23] V. V. Jouikov, *Electrochemical reactions of organosilicon compounds*, Russ. Chem. Rev. 2007, 66, 509-540.

[24] M. Okano, K. Watanabe, *Electrochemical synthesis of stannanesilane and stannanegermane copolymers*, Electrochem. Commun. 2000, 2, 471-474.

[25] K. Subramanian, *A Review of Electrosynthesis of Polysilane*, Polym. Rev. 1998, 38, 637-650.

[26] L. A. Vermeulen, K. Smith, J. Wang, *Electrochemical polymerization of alkyltrichlorosilane monomers to form branched Si backbone polymers*, J. Electrochim. Acta 1999, 45, 1007-1014.

Study of the polarization effect on ultraviolet absorption of corannulene molecules in solution

Nadiia Pastukhova[a,*], Layla Martin-Samos[a], Laura Zoppi[b], Egon Pavlica[a]

[a]*University of Nova Gorica, Vipavska 13, SI-5000 Nova Gorica, Slovenia*
[b]*CNR-IOM DEMOCRITOS, Istituto Officina dei Materiali, c/o SISSA Scuola Internazionale Superiore di Studi Avanzati, Via Bonomea 265, 34136 Trieste Italy*

Abstract

Corannulene is the smallest bowl-shaped fullerene fragment with very promising electrical and optical properties, where was theoretically predicted intermolecular charge transport mediated by super atomic molecular orbitals. We have studied polarization effect of solvent on this promising molecule using the absorption spectra of corannulene solutions. We measured ultraviolet absorption of corannulene solutions in chloroform, dichloromethane and diethyl ether. The study of absorption peaks was compared to theoretical model. We identified peaks at E=4.20 eV and E=4.31 eV as possible exitations to super atomic molecular orbital. We calculated polarization effect of non-polar solvents: chloroform - 0.017 eV, diethyl ether - 0.013 eV, and dichloromethane - 0.01 eV.

Keywords: corannulene, super atomic molecular orbital (SAMO), UV absorption, solvent polarization

1. Introduction

Organic semiconductors (OS) are promising materials for the future of electronics. They are already in use for many devices such as: organic light-emitting displays (OLED), organic field-effect transistors (OFETs) [1, 2, 3], organic photovoltaic cells (OPVs) [4, 5], memristors [6], sensors for medicine and sports [7], electronic textile and yarns [8, 9]. Although OS exhibits attracting capabilities, their charge carrier mobility is still relatively

---

[*]Corresponding author
Email address: `nadiia.pastukhova@ung.si` (Nadiia Pastukhova)

low compared to Si based electronic materials. Main reason for low mobility is the disorder of molecular orientation that is set up during thin film deposition. This can be exemplified by comparing a single crystal of poly(3-hexylthiophene) (P3HT) where the mobility of charge carriers is significantly higher in comparison to spin-coated thin films [18, 19]. This phenomenon happens because of the absence of molecular orbital overlapping in thin film.

To achieve better orbital overlapping could be use the materials with extremely large molecular orbitals, which are expanding beyond the Van der Waals radius of the molecule. Super atomic molecular orbitals (SAMO) are unconventional orbitals that arise from the central potential of the molecular cavity, evoking well-defined hydrogenic s, p, and d orbital angular momentum shapes that extend beyond the molecule but are bound by a shallow potential at the center of the hollow structure [10]. Scanning tunneling microscopy (STM) and density functional theory (DFT) were used to explore the relation between the nearly spherical shape and unoccupied electronic structure of buckminsterfullerene (C_{60}) molecules adsorbed on copper surfaces. This was first experimental evidence of SAMO state [11]. The physical origin of SAMOs is ascribed to many body screening and polarization effects, typical of a polarizable assembly (e.g., graphene) that is important for accurate prediction of electronic properties involving these diffuse orbitals [13]. Corannulene ($C_{20}H_{10}$) is the smallest bowl-shaped fullerene fragment with very promising electrical and optical properties, where intermolecular charge transport mediated by SAMO was theoretically predicted[10]. In this molecule SAMO have not been experimentally explored yet. In order to experimentally confirm the existence of SAMO orbital in disordered thin layers of corannulene, we measure ultraviolet (UV) absorption to check how the solvent influence the absorption peaks. We expect that varying solvent should influence SAMO peak differently compared to exciton peak. In this study we compared a theoretical calculations of absorption of a single molecule of corannulene in vacuum to experimentally obtain spectra of light absorption for corannulene molecules in solution. This helped us to estimate the polarization effect of different solvents on corannulene molecules. We considered molecule of corannulene in solution and molecules of solvent as harmonic oscillators. The atom in interaction with electromagnetic field behaves like a set of classical oscillators with the natural frequencies equal to the frequencies of transitions between atomic energy levels. This means that each transition between atomic states, and is associated with the oscillator. We report how oscillator strength changed and how strong is the polarization effect of organic

2

solvents on corannulene in solutions.

2. Experimental setup

2.1. Sample preparation

Corannulene was synthesized by group of Jay S. Siegel [20]. Solutions with different concentrations were prepared from corannulene powder in chloroform $CHCl_3$, dichloromethane CH_2Cl_2 (both Sigma-Aldrich) and diethyl ether $(C_2H_5)_2$ (Alfa Aesar). These solvents were chosen based on their UV cutoff and corannulene solubility. Corannulene solutions were prepared by dilution from saturated solution. Diluted solutions were sonicated 5 minutes before each dilution. We present a table with calculated concentrations (Table 1).

Table 1: Concentrations of corannulene solutions in chloroform, dichloromethane and diethyl ether used for measurements of ultraviolet absorption. Last column UV cutoff of these solvents.

Concentration Solvent	C1 μg/mL	C2 μg/mL	C3 μg/mL	C4 μg/mL	C5 μg/mL	UV cutoff nm
Chloroform	10	5	2.5	1	na	240
Dichloromethane	26	13	5.2	2.6	1.3	230
Diethyl ether	2.8	1.87	1.4	0.93	0.7	220

2.2. Absorption measurements

The absorption spectra of corannulene in three solutions with concentrations from 0.7 μg/mL to 26 μg/mL were measured. Absorption measurements were performed using spectrophotometer Perkin Elmer Lambda 650S. Two cuvettes (Hellma 114-QS) with light path of 10 mm and volume of 1400 μl were used for the experiment. Clear solvents were measured for background removal. Solutions were sonicated for 5 minutes to avoid molecules aggregation. Absorption of pristine solvent, which was used as a reference, was subtracted from the absorption of solution. Each spectrum is reported as an average of 3-10 repetitions. Number of repetitions was chosen depending on the absorption level of solution in order to reduce noise to signal ratio.

2.3. Theoretical calculations

Theoretical investigation of SAMOs requires methods that include Many-Body Perturbation Theory [17]. We have customized a hybrid methodology based on plane-wave DFT formalism (Quantum-ESPRESSO) and Many-Body Perturbation Theory (MBPT) in the GW approximation (SAX). The DFT wave function is used to initiate the solving of nonself- consistent Dyson-like equations for electronic screening and one particle electronic Green function. Within the GW approximation the self-energy is determined as the product of a single-particle Green function, G, and a nonlocal and dynamically screened Coulomb potential. One can still refer to single-particle energy levels; however, particles are quasi-particles (QP) renormalized for screening effects due to the presence of all other particles. GW and HartreeFock (HF) self-energies are very similar in that, in practice, the GW self-energy contains a HF term in addition to a pure polarization term, which includes the dielectric response of the electronic gas. In principle, the GW self-energy should be evaluated self-consistently. However, due to the high computational demands of such an approach, a non-selfconsistent scheme, that is, G0W0, with the initial G0 obtained from DFT, is standard for practical calculations, and is also the scheme adopted in this work. In this framework, exchange and Many-Body polarization effects critical for describing SAMOs properties are properly accounted for.

3. Results

The absorption spectrum of 10 μg/mL of corannulene in chloroform, 26 μg/mL of corannulene in dichloromethane and 2.8 μg/mL of corannulene in diethyl ether are shown in Fig. 1. Each spectrum exhibits a group of peaks in the energy range from 3.5 eV to 4.75 eV. The highest intensity peak for all spectra is centered around 4.3 eV with a shoulder on the high energy side. Shoulder occurs at the 4.5 eV and a low energy tail extends from 4.0 eV to 3.5 eV. The evolution of absorption features was studied as a function of concentration of corannulene in dichloromethane (Fig. 2b), chloroform (Fig. 2c) and diethyl ether (Fig. 2d). To accurately determine behavior of absorption transitions on solvent, each solution absorption spectrum was fit to four Gaussian peaks (Fig. 2a) with the parameters provided in Table 2 for similar concentration of corannulene around 2.6 μg/mL for each solvent. We explored dependence of amplitude of peaks on concentration, and identify linear dependence on it. This means there was no aggregation of molecules and solute was well dissolved and mixed [15].
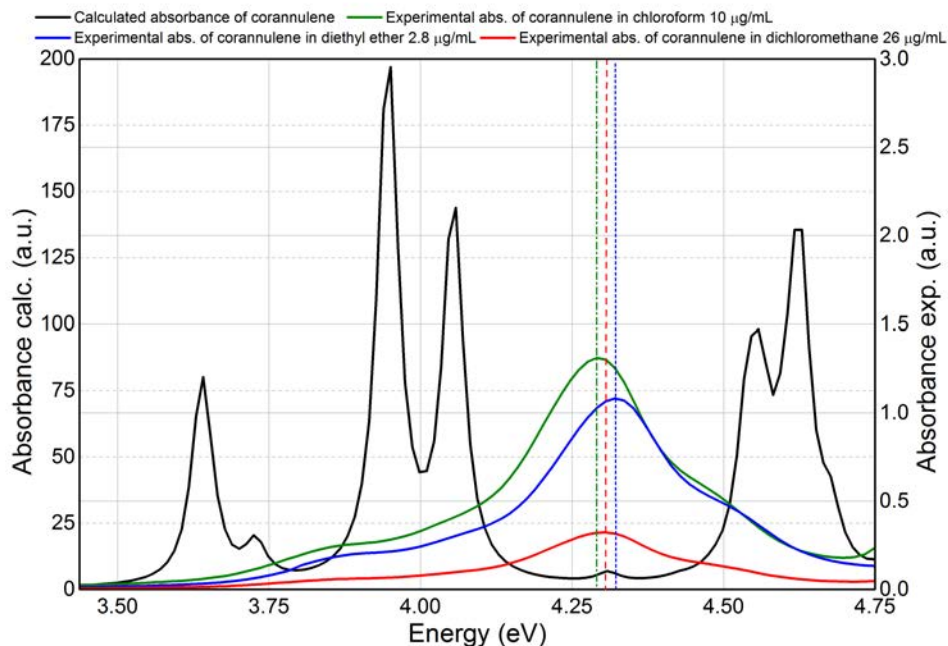
4

Figure 1: Absorption spectra of 10 μg/mL solution of corannulene in chloroform (green solid line), 26 μg/mL solution of corannulene in dichloromethane (red solid line), 2.8 μg/mL solution of corannulene in diethyl ether (blue solid line) and GW-BSE-predicted optical absorption spectrum of corannulene single molecule in vacuum (black solid line). Vertical dashed lines show energies of main peak E=4.295 eV for solution in chloroform, E=4.303 eV for solution in dichloromethane, and E=4.323 eV for solution in diethyl ether. GW-BSE-predicted energy of this peak is at E=4.31 eV.

The energy position of peaks is present in (Table 2) for different solvents. The peaks exhibits different center positions in different solvents [16]. The shift of the peaks does not show any significant correlation with the solvent. We studied the dependence of the E=3.85, 4.20, 4.31 and 4.50 eV area under the peak, which is proportional to the transition oscillator strength as a function of corannulene concentration in three solvents. We used model oscillator strength = slope × concentration. Slope of oscillator strength is independent on the concentration for four peaks as a function of dipole moment shown in (Fig. 2). Dipole moment for chloroform is 1.1, for diethyl ether is 1.3 and for dichloromethane is 1.8. Peak 2 and peak 3 are showing significantly different change in slope for the solvents with dipole moment 1.1 and 1.3. This could be a signature of SAMO state, which is the most extend orbital in corannulene and should exhibits the highest effect
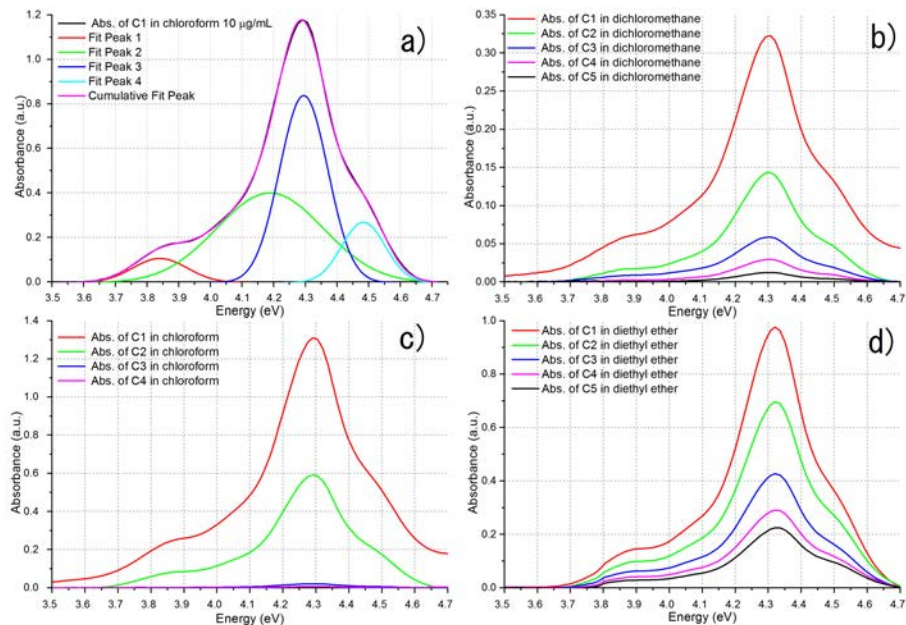
Figure 2: a) This is comparison between measured spectra and modeled spectra, which is composed of four Gaussian peaks. The modeled spectra reproduces measurements. The parameters of the modeled spectra are shown in Table 2. b) absorption spectra of different concentrations of corannulene in dichloromethane solutions which are marked in Table 1, c) absorption spectra of different concentrations of corannulene in chloroform solutions (Table 1), d) absorption spectra of different concentrations of corannulene in diethyl ether solutions (Table 1).

on polarization. Experimental spectra was compared to theoretically calculated absorption spectrum which is shown in Fig. 1 as black solid line. Dominant absorption peaks with E=3.64 eV, E=3.95 eV, E=4.06 eV, E=4.56 eV, E=4.63 eV from calculated spectra are negligible in the measured spectrum. Peaks with calculated high intensity (4.0 eV and 4.5 eV) are probably present in the experimental spectrum, but are highly overlapped by neighboring peaks. In contrast, peak of low amplitude in calculated spectrum E=4.31 is found experimentally as the highest amplitude peak. Theoretical calculation predicts the center of the SAMO peak to be at 4.31 eV. According to the calculation results, absorption of a photon is highly unlikely and the absorption is low. However the measured absorption exhibits the highest peak which is centered relatively near the theoretically predicted SAMO peak. The influence of solvent on this peak relative to its center is 17 meV,

Table 2: Each spectrum was modeled to four Gaussian shapes. For each solvent was chosen similar concentration of corannulene in solution around 2.6 μg/mL. For each Gaussian curve, the peak energy and full width at half maximum (FWHM) are indicated.

Peak energy	Peak1	Peak2	Peak3	Peak4
Chloroform	3.770(5)	4.22(1)	4.293(1)	4.486(4)
Dichloromethane	3.854(5)	4.26(8)	4.3000(8)	4.50(2)
Diethyl ether	3.861(3)	4.19(1)	4.3231(8)	4.513(2)
FWHM				
Chloroform	0.14(1)	0.46(2)	0.184(4)	0.14(1)
Dichloromethane	0.14(1)	0.42(1)	0.169(4)	0.131(8)
Diethyl ether	0.171(9)	0.41(3)	0.185(3)	0.159(7)

13 meV and 10 meV in chloroform, diethyl ether, and dichloromethane respectively. The highest shift occurs in solvent with lowest dipole moment and vice versa. Therefore we can conclude that the dipole moment of the solvent shifts the peak center, which could represents the result of the interaction between solvent dipole field and SAMO.

4. Conclusions

Using the absorption spectra of corannulene solutions we have studied polarization effect of solvent on this molecule. Based on the concentration dependence, the aggregation of molecules was excluded. Corannulene exhibits high solubility in chloroform, diethyl ether and dichloromethane up to 26 μg/mL. We identified peaks at E=4.20 eV and E=4.31 eV as a possible exitations to the super atomic molecular orbital. We compared experimentally measured absorption spectra with theoretically calculated absorption spectrum. The estimated polarization effect was redshift of 17 meV, 10 meV and blueshift 13 meV in chloroform, dichloromethane and diethyl ether respectively.

References

[1] A. Tsumura, H. Koezuka, T. Ando, *Macromolecular electronic device: Field-effect transistor with a polythiophene thin film* Appl. Phys. Lett., 49, 1210-1212, 1986.
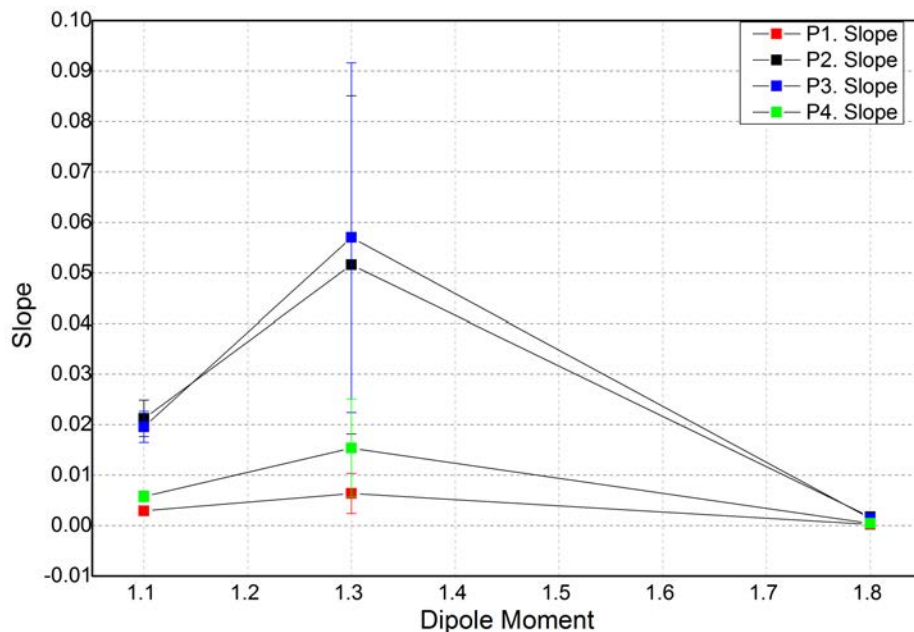
Figure 3: Slope of oscillator strength independent on concentration for four peaks as a function of dipole moment. Dipole moment for chloroform is 1.1, for diethyl ether is 1.3 and for dichloromethane dipole moment is 1.8. For the Peak 2 and Peak 3 slope sharply increase compared to the Peak 1 and Peak 4 for the solvents with dipole moment 1.1 and 1.3.

[2] Y. Y. Lin, D. J. Gundlach, S. F. Nelson, T. N. Jackson, *Stacked pentacene layer organic thin-film transistors with improved characteristics* IEEE Electron Device Lett, 18, 606, 1997.

[3] H. Minemawari, D.J. Yamada, H. Matsui, J. Tsutsumi, S. Haas, R. Chiba, R. Kumai, T. Hasegawa, *Inkjet printing of single-crystal films*, Nature, 475, 7356, 36-47, 2011.

[4] Y. Yamada, T. Nakamura, M. Endo, A. Wakamiya, Y. Kanemitsu, *Photocarrier recombination dynamics in perovskite CH3NH3PbI3 for solar cell applications*, J. Am. Chem. Soc., 136, 33, 116-103, 2014.

[5] J. Burschka, N. Pellet, S.-J. Moon, R. Humpry-Baker, P. Gao, M. K. Nazeeruddin, M. Grtzel, *ISequential deposition as a route to high-performance perovskite-sensitized solar cells*, Nature, 499, 7458, 31-69, 2013.

[6] R.E. Pino, *Memristor-based synapse design and training scheme for neuromorphic computing architecture*, The 2012 International Joint Conference on Neural Networks (IJCNN), 1-5, 2012.

[7] A.K. Bansal, S. Hou, O. Kulyk, E.M. Bowman, I.D. Samuel, *Wearable Organic Optoelectronic Sensors for Medicine*, Adv. Mater., 2014.

[8] R. Ramanathan, A.E. Kandjani, S. Walia, S. Balendhran, S.K. Bhargava, K. Kalantar-zadeh, V. Bansal, *3-D nanorod arrays of metalorganic KTCNQ semiconductor on textiles for flexible organic electronics*, Adv. Mater., RSC Adv., 3, 39, 17654, 2013.

[9] M. Barbaro, A. Caboni, P. Cosseddu, G. Mattana, A. Bonfiglio,*Active devices based on organic semiconductors for wearable applications*, IEEE Trans. Inf. Technol. Biomed., 14, 3, 758-66, 2010.

[10] L. Zoppi, L. Martin-Samos, K. K. Baldridge, *Buckybowl superatom states: a unique route for electron transport?*, Phys. Chem. Chem. Phys., 17, 8, 6114-6121, 2015.

[11] M. Feng, J. Zhao, H. Petek, *Atomlike, Hollow-CoreBound Molecular Orbitals of C60*, Science, 320(5874), 359-62, 2008.

[12] L. Zoppi, L. Martin-Samos, K. K. Baldridge, *Structure-Property Relationships of Curved Aromatic Materials from First Principles*, Acc. Chem. Res., 47 (11), 3310-3320, 2014.

[13] V.M. Silkin, J. Zhao, F. Guinea, E. V. Chulkov, P. M. Echenique, H. Petek,*Image potential states in graphene*, Phys. Rev. B, 80, 121, 408, 2009.

[14] A. Pivrikas, G. Juska,*Charge carrier transport and recombination in bulk-heterojunction solar-cells*, Proc. SPIE, 59380N-11, 2005.

[15] V. Bulovic, P.E. Burrows, S.R. Forrest, J.A. Cronin, M. E. Thompson, *Study of localized and extended excitons in 3,4,9,10-perylenetetracarboxylic dianhydride (PTCDA) I. Spectroscopic properties of thin films and solutions.*, Chemical Physics, 210, 1-12. 1996.

[16] E. Herbert Ungnade, *The Effect of Solvents on the Absorption Spectra of Aromatic Compounds*, J. Am. Chem. Soc., 75 (2), 432-434, 1953.

[17] G. Onida, L. Reining, A. Rubio, *Electronic excitations: Density-functional versus Many-Body Greens-function approaches.*, Rev. Mod. Phys., 74, 601-659, 2002.

[18] M. Hufnagel, M. Thelakkat, *Simultaneous Morphological Stability and High Charge Carrier Mobilities in Donor-Acceptor Block Copolymer/PCBM Blends*, Journal of Polymer Science Part B: Polymer Physics, 54 (12), 1125-1136, 2016.

[19] M. L. Jones, D. M. Huang, B. Chakrabarti, C. Groves, *Relating Molecular Morphology to Charge Mobility in Semicrystalline Conjugated Polymers*, J. Phys. Chem. C, 120 (8), 4240-4250, 2016.

[20] T. J. Seiders, E. L. Elliott, G. H. Grube, J. S. Siegel, *Synthesis of Corannulene and Alkyl Derivatives of Corannulene*, J. Am. Chem. Soc., 121 (34), 7804-7813, 1999.